Faculty of Science
University of Helsinki

SAFETY AND QUALITY IN ASSOCIATION WITH CLINICAL MAGNETIC RESONANCE IMAGING - APPLICATIONS IN STRUCTURAL MRI AND SIMULTANEOUS EEG-FMRI

Linda Kuusela

Department of Physics
Faculty of Science
University of Helsinki

HUS Medical Imaging Center
University of Helsinki and
Helsinki University Hospital

ACADEMIC DISSERTATION

Doctoral dissertation, to be presented for public discussion with the permission
of the Faculty of Science of the University of Helsinki,
in Auditorium A110 in Chemicum building at the Kumpula Campus, Helsinki,
on the 23rd of October, 2020 at 1 p.m.

Helsinki 2020

Supervisors:
Professor Sauli Savolainen
Department of Physics
University of Helsinki
Finland
and
HUS Medical Imaging Center
Helsinki University Hospital
Finland

Official reviewers:
Professor Petro Julkunen
Department of Applied Physics
University of Eastern Finland
Finland
and
Department of Clinical Neurophysiology
Kuopio University Hospital
Finland

Adjunct Professor Mika Kapanen
Department of Medical Physics
Tampere University Hospital
Finland

Opponent:
Adjunct Professor Eveliina Lammentausta
Department of Diagnostic Radiology
Oulu University Hospital
Finland

The Faculty of Science uses the Urkund system (plagiarism recognition) to examine all doctoral dissertations.

ISSN 2669-882X (printed)
ISSN 2670-2010 (e-publication).

ISBN 978-951-51-6630-2 (paperback)
ISBN 978-951-51-6631-9 (PDF)
Unigrafia
Helsinki 2020

ABSTRACT

Magnetic resonance imaging (MRI) technology is rapidly developing in acquisition, reconstruction and post-processing. When introducing novel methods to clinical routine, there may be aspects of the method that hinder its application. These aspects comprise safety issues, restrictions on the use of equipment, long scan times or time-consuming data post-processing, or combinations of these. Obviously, these issues must be eliminated or managed. The work presented in this thesis was driven by clinical needs at HUS Helsinki Medical Imaging Center, Finland.

In simultaneous electroencephalography (EEG) and functional MRI (fMRI) the equipment is MRI-compatible and the use of only a certain low specific absorption rate (SAR) imaging sequences are allowed. The requirements for performing a simultaneous EEG-fMRI study are safety, good signal stability, acceptable signal-to-noise (SNR) ratio and no significant image artifacts. Both temperature measurements, and image quality assessments were carried out. The highest temperature changes were observed for the sequence with the highest SAR, this was, however, within acceptable limits for safe scanning. A decrease in SNR was observed with the fMRI sequence.

In craniosynostosis imaging, the aim is to diagnose prematurely closed skull suture of the growing skull. The gold standard of craniosynostosis imaging is computed tomography (CT), but a non-ionizing modality enabling anatomical imaging in the same imaging session was clinically desired. Thus, a black bone MRI (BB-MRI) sequence was developed based on research reported by others and further optimized for the specific needs of our hospital. To produce the 3D rendered image, a segmentation algorithm based on a bias field-corrected fuzzy c-means algorithm was used. To verify the reliability of the BB-MRI, a comparison study with CT was conducted, where sutures and intracranial impressions were rated. For the assessment of sutures, the inter-rater reliability was observed to be high with both BB-MRI and CT. For the assessment of intracranial impression, the inter-rater reliability was low with both modalities.

Gradient Echo Plural Contrast Imaging (GEPCI) is a post-processing technique, which produces quantitative information as well as several image contrasts. The issue with GEPCI is the relatively long scan time; 8-12 minutes, depending on the resolution and stack coverage. The usability of partial Fourier (PF) technique was studied with both phantom and volunteer measurements. PF factor in only the phase direction should be used, yielding a reduction in scan time of 24%.

Keywords: Magnetic resonance imaging, functional magnetic resonance imaging, simultaneous EEG-fMRI, image quality, advanced neuroimaging, craniosynostosis, black bone, segmentation, multi-contrast imaging

ACKNOWLEDGMENTS

This research was carried out at the HUS Medical Imaging Center and was supported by the State Subsidy for University Hospitals. Additional financial support was received from Svenska kulturfonden.

I am sincerely grateful to my supervisor, Professor Sauli Savolainen, for his unwavering encouragement and patience.

I thank the official reviewers of this thesis, Professor Petro Julkunen and Adjunct Professor Mika Kapanen, for invaluable and constructive comments that greatly improved the final product. Adjunct Professor Eveliina Lammentausta is warmly thanked for accepting the invitation to be my opponent at the public defense of this dissertation.

I am indebted to the coauthors of the adjoining publications. I particularly thank Adjunct Professor Outi Sipilä, for her insight into everything involving academic research and for the effort put into the simultaneous EEG-fMRI project, and Sampsa Turunen, for his expertise in electroencephalography and witty humor. I thank everyone involved in the craniosynostosis project, especially the driving force, Adjunct Professor Anne Saarikko. Warm thanks also to principal investigator Antti Korvenoja and master coder Riikka Ruuth of the multicontrast imaging research project.

I thank all of my colleagues, especially Marjut Timonen and Viljami Sairanen, for their contributions. Also thanked are the radiographers and radiologists of the HUS Helsinki Medical Imaging Center.

I am also deeply grateful to my nearest and dearest for enabling me to do all the things that I've wanted, even in the extremely rough patches. I particularly thank Timo, my bearded personal travel planner and companion; we have had some crazy rides and dives. By finally finishing this thesis, I admit that I have lost an old bet. Robin Hood, I think I owe you a snowboarding trip.

Vantaa, August 2020

Linda Kuusela

Contents

LIST OF ORIGINAL PUBLICATIONS

This thesis is based on the following publications:

I **Kuusela, L**., Turunen, S., Valanne, L. & Sipila, O. 2015. Safety in simultaneous EEG-fMRI at 3 T: temperature measurements. Acta Radiologica, pp. 739-745

II Ihalainen, T., **Kuusela, L**., Turunen, S., Heikkinen, S., Savolainen, S. & Sipila, O. 2011. Data quality in fMRI and simultaneous EEG-fMRI. Magnetic Resonance Materials in Physics, Biology and Medicine, pp, 23-31

III **Kuusela, L**., Hukki, A., Brandstack, N., Autti, T., Leikola, J. & Saarikko, A. 2018. Use of black-bone MRI in the diagnosis of the patients with posterior plagiocephaly. Child's Nervous System, pp. 1383-1389

IV Saarikko, A., Mellanen, E., **Kuusela, L**., Leikola, J., Karppinen, A., Autti, T., Virtanen, P. & Brandstack, N. 2020. Comparison of Black Bone MRI and 3D-CT in the preoperative evaluation of patients with craniosynostosis. Journal of Plastic, Reconstructive & Aesthetic Surgery, pp. 723-731

V Ruuth, R., **Kuusela, L**., Mäkelä, T., Melkas, S. & Korvenoja, 2019. A. Comparison of reconstruction and acquisition choices for quantitative T2* maps and synthetic contrasts. European journal of radiology open, pp. 42-48

These studies are referred to by Roman numerals I-IV throughout the document. Study **I** is reprinted with permission from SAGE Publications. Studies **II** and **III** by permission from Springer Science and Business Media, Studies **IV** and **V** by Elsevier Ltd.

AUTHOR'S CONTRIBUTION

In Study **I**, the author performed all experiments, performed the analysis, and drafted the manuscript. In Study **II**, the author performed all simultaneous EEG-fMRI experiments, including the volunteer measurements, and drafted the manuscript. Study **II** was included in the thesis by Toni Ihalainen (Quality control methods for magnetic resonance imaging in a multi-unit medical imaging organization, 2016). In Study **III**, the author optimized the sequence/protocol used, scripted the segmentation algorithm, performed all image data processing, and drafted the manuscript. In Study **IV**, the author optimized the sequence/protocol used, scripted the segmentation algorithm, performed all the image data processing and drafted the manuscript. In Study **V**, the author designed and performed all experiments and drafted the manuscript.

ABBREVIATIONS

α	flip angle
ACR	American College of Radiology
$\boldsymbol{B_0}$	static magnetic field strength, also known as magnetic flux density
$\boldsymbol{B_1}$	radiofrequency field
BCFCM	bias field-corrected fuzzy c-means clustering
BOLD	blood oxygen level dependent signal
BW	bandwidth
CT	computed tomography
D	duty cycle
dMRI	diffusion magnetic resonance imaging
ECG	electrocardiography
EEG	electroencephalography
EOG	electrooculography
EPI	echo planar imaging
fBIRN	functional Biomedical Informatics Research Network
FFT	fast Fourier transform
FID	free induction decay
FM	frequency mask
fMRI	functional magnetic resonance imaging
FSL	FMRIB Software Library
GE	gradient echo
GEPCI	gradient echo plural contrast imaging
IP	in-phase
IR	inversion recovery
ME	multi echo
MRI	magnetic resonance Imaging
NEX	number of excitations
OOP	Out-of-phase
PF	partial Fourier
PFP	partial Fourier in the phase encoding direction
PFS	partial Fourier in the slice encoding direction
PROPELLER	periodically rotated overlapping parallel lines with enhanced´ reconstruction
ρ	proton density
RF	radio frequency
ROI	region of interest
RT	radiation therapy
SAR	specific absorption rate
SE	spin echo
SNR	signal-to-noise
SWI	susceptibility weighted image

T_1	T_1 relaxation
T_2	T_2 relaxation
T_2*	T_2* relaxation
TE	time of echo
TSE	turbo spin echo
TR	time of repetition
UTE	ultra short TE
VIBE	Volumetric Interpolated Breath-hold Examination

1 INTRODUCTION

Magnetic resonance imaging (MRI) is a widely used imaging modality in clinical settings and research. MRI has a good soft tissue contrast and it is possible to change the image contrast by changing the sequence type and parameters. In addition to structural imaging, functional imaging is possible. The MRI technology is rapidly developing in acquisition, reconstruction, and image post-processing. When introducing novel methods to clinical routine, there may be aspects of the method that hinders its application. These aspects comprise safety issues, restrictions to use of equipment, long scan times, time-consuming data post-processing, or a combination of these. Obviously, these issues must be eliminated or managed for the methods to become clinical practice.

MRI does not use ionizing radiation, but safety is still an essential concern. The most significant safety issue is caused by unintended introduction of ferromagnetic objects to the MRI scanner's strong static magnetic field, which will lead to the object being drawn to the magnet (Sammet, 2016). A radio frequency (RF) field is used for excitation of proton spins. The energy of the RF field is absorbed by an object and has the potential to increase object's temperatures. These issues must be taken into account when introducing equipment to the MRI environment, e.g. when electroencephalography (EEG) equipment is going to be used in a functional MRI (fMRI) study.

Depending on the clinical needs, an MRI study may last from 5 minutes to several hours. The total scan times are relatively long because the acquisition technique is time-consuming and several imaging sequences with different contrasts are acquired, or in advanced applications a large amount of data is required for analysis; e.g. for gradient echo plural contrast imaging (GECPI), the post-processing technique requires data with multiple echoes (Luo et al., 2012). To produce a time-efficient protocol, the sequences are optimized based on the diagnostic requirements and there is always a tradeoff between resolution, signal-to-noise (SNR), and scan time. In real life, the tradeoff is much more complex and dependent on the consistency of the tissue and subject movement. When imaging *in vivo,* subject motion might be an issue. When imaging children in natural sleep, motion can be reduced by using sequences with lower acoustic noise levels (Zhu et al., 2020). There are also sequences with motion compensation (Pipe, 1999). As new imaging sequences emerge, the usability of these must be assessed in a clinical setting and compared with current imaging methods.

Automatic post-processing can ease the introduction of the method to clinical use. The post-processing of medical images is dependent on the modality in question. In the segmentation of MRI images, one must account for modality-specific image artifacts, e.g. intensity variations across image space.

The work presented in this thesis was motivated by clinical needs. To introduce new imaging methods, three important aspects must be taken into consideration: safety, stable image quality, and reliable outcome. This includes assessment of heating in simultaneous EEG-fMRI (Study **I**), image quality assessment in simultaneous EEG-fMRI and GEPCI (Studies **II** and **V**), sequence optimization for craniosynostosis imaging and GEPCI (Studies **III**, **IV** and **V**) and development of post-processing methods for visualizing skull structures for craniosynostosis diagnostics (Studies **III** and **IV**).

1.1 SIMULTANEOUS EEG-FMRI

In EEG the electrical activity of the brain is measured as electric potential difference fluctuations in a set of electrodes placed on the scalp. The potential differences are due to synchronous postsynaptic potentials (Partanen & Cheour, 2006, p. 50). With fMRI it is possible to study the blood oxygen level-dependent (BOLD) signal. The changes in BOLD signal are due to increased concentration of oxygenated hemoglobin, which has a small effect on the relaxation time and consequently on the measured signal. The oxygenated hemoglobin concentration will rise with increased neuronal activity (Jezzard et al., 2003, pp. 11–12).

In simultaneous EEG-fMRI data are collected with both modalities at the same time taking advantage of the high temporal resolution of EEG and high spatial resolution of fMRI. Because the EEG and fMRI data is acquired simultaneously, there is a natural co-registration of the data, and no discrepancy in task execution, subject alertness or the environment, in comparison to separate data collection (Debener et al., 2006b). Simultaneous EEG-fMRI is used clinically for localizing interictal activity foci. The statistical analysis of fMRI data is based on the timings of interictal activity observed in the EEG (Ives et al., 1993). In research, simultaneous EEG-fMRI is used to study resting state networks and connectivity (Brueggen et al., 2017; Dong et al., 2016), but also task-based studies are under active research (Debener et al., 2006a; Li et al., 2020; Michels et al., 2010; Zich et al., 2015; Zotev et al., 2018).

In simultaneous EEG-fMRI, MRI conditional EEG equipment is used and there are restrictions on which imaging sequences can be applied. These restrictions are due to the possible heating of the electrodes. For diagnostic imaging, a larger variety of sequences may be needed. To extend the capabilities to use a wider range of sequences, the safety of the sequences must be assessed. Moreover, EEG equipment can affect the image quality, and therefore, it must also be assessed. MRI also affects the EEG, causing artifacts in the collected EEG, which have to be corrected to get diagnostic EEG (Allen et al., 2000; Debener et al., 2008). EEG correction methods will not be discussed in this thesis.

1.2 CRANIOSYNOSTOSIS IMAGING WITH MRI

Imaging of osseous tissue with MRI is challenging, because of the small concentrations of water, and hence, the low signal yield. Because of the versatility of the modality, there is an interest in imaging osseous tissue with MRI e.g. with craniosynostosis imaging, hybrid positron emission tomography MRI scanner (Berker et al., 2012; Kim et al., 2012) and radiation therapy (RT) planning (Johnstone et al., 2018).

Craniosynostosis refers to the premature closing of the skull sutures, which hinders the skull from expanding normally as the brain grows and results in skull deformities (Albright & Byrd, 1981; Persing, 2008). Synostosis can in most cases be diagnosed by a physical examination, and computed tomography (CT) is currently the primary imaging modality for diagnosing craniosynostosis (Fearon et al., 2007; Kirmi et al., 2009; Nagaraja et al., 2013; Persing, 2008). In addition to suture patency the CT images reveal intracranial impressions, which are small dents on the inner surface of the skull and are considered a tell-tale sign of increased intracranial pressure (Agrawal et al., 2007; Tuite et al., 1996).

Eley et al. (2012) introduced a novel black bone MRI (BB-MRI) for craniosynostosis imaging. They introduced an in-phase 3D gradient echo (GE) image acquisition, where the signal from the skull is suppressed and otherwise strive to a uniform signal intensity in non-osseous tissue. The images are then thresholded for 3D visualization of the skull bones (Eley et al., 2013, 2014; Eley, McIntyre, et al., 2012; Eley, Watt-Smith, et al., 2012). A non-ionizing imaging method of craniosynostosis is valuable because of the young age of the patients and potential follow-up scans needed. Children are also known to be more sensitive to radiation (Brenner et al., 2007; Frush et al., 2003; Pearce et al., 2012). MRI has a better soft tissue contrast than CT, potentially revealing soft tissue pathologies in the same session as acquisition of skull images. For instance, Chiari malformation is a frequently occurring pathology in syndromic synostosis (Hukki et al., 2012; Leikola et al., 2010).

For diagnosing craniosynostosis 3D rendered skull images are generated from CT images and this visualization is based on thresholding. With MRI the thresholding might not be adequate because of the typical image artifacts present in MRIs, e.g. intensity bias fields, Gibbs ringing, and chemical shift artifacts. These artifacts can complicate the segmentation and thresholding might not work adequately.

Patients with suspected craniosynostosis are mainly infants or toddlers, but because follow-up is required older children are also imaged. The consistency and size of the skull and brain tissue of an infant are markedly different from the corresponding structures of 7-year-olds. The large variation in age will have an impact on skull consistency and structures of interest, which is a challenge for segmentation. Thus, automatic image segmentation pipeline, which takes into account the disadvantageous

properties of MRI images, might also be preferred. The automatic segmentation will also decrease the time spent on manual post-processing.

1.3 MULTI-CONTRAST IMAGING

In an MRI study, a set of sequences with different contrasts is acquired. The contrasts are chosen based on clinical application. In multi-contrast MRI from one sequence, several image contrasts can be calculated, and the benefit is a reduced total scan time. Also, the images are by default co-registered i.e. in the same image orientation and resolution (Luo et al., 2012). Several multi-contrast imaging and reconstruction methods have been introduced. GEPCI is a post-processing technique of a multi-echo (ME) 3D GE sequence, which was first introduce by Yablonskiy (as cited in Luo et al., 2012) and the method utilizes both magnitude and frequency (phase) information. Usually, only the magnitude information is used in image reconstruction. With GEPCI reconstruction, it is possible to a produce quantitative T_2*-relaxation map as well as susceptibility weighted images (SWI), fluid suppressed T_2*-weighted images, T_1-weighted images, and frequency maps (Bashir & Yablonskiy, 2006; Luo et al., 2012; Yablonskiy et al., 2013). The GEPCI technique has been successfully used in assessing damage in images of multiple sclerosis (Luo et al., 2014; Sati et al., 2010; Wen et al., 2015), and Alzheimer's disease (Fagan et al., 2017). At our hospital, the GEPCI sequence is used in the research study protocol for traumatic brain injury and small vessel disease.

The sequence is relatively fast due to only one excitation RF pulse and the low flip angle. Yet, collecting data with sufficiently high resolution and several TEs is very time-consuming and can result in scan times of 8-12 minutes (Luo et al., 2012; Ruuth et al., 2019). The 3D sequences are especially susceptible to motion artifacts. If the subject moves during the acquisition, the movement artifacts will affect the image quality of the whole stack (Bushberg et al., 2002, p. 439) and may result in nondiagnostic images. To reduce the scan time, several imaging acceleration techniques have been developed, which are based either gathering less data into the k-space or filling the k-space faster with refocusing pulses or gradients. The imaging acceleration techniques also have downsides of blurring, reduced SNR, distortions, or other artifacts (McRobbie et al., 2005, pp. 132,221-225,320-321). This must be factored into the optimizing process.

2 AIMS OF THE STUDY

The aim of this dissertation was to ease the application of imaging and post-processing methods in a clinical setting. The studies were designed to:

1. Investigate the possibility of using a wider range of sequences in a simultaneous EEG-fMRI imaging session by temperature measurements of MRI-compatible EEG caps because safety is of the utmost importance and must be ensured (Study **I**).

2. Ensure a well-tested and optimized imaging protocol for sufficient and stable image quality. The impact of the EEG equipment, used in a simultaneous EEG-fMRI study, on the image quality was assessed (Study **II**). The optimization of the sequence used for craniosynostosis imaging was performed by assessing the output of the segmentation algorithm (Studies **III** and **IV**). The multicontrast imaging sequence was investigated for the possibility to reduce the scan time while preserving the quantitative values and image quality (Study **V**).

3. Develop a segmentation algorithm with minimal user intervention to ease the clinical use of the BB-MRI sequence (Studies **III** and **IV**).

3 THEORY

This section is divided into five subsections. Section 3.1 includes a short introduction to MRI, but a more detailed theory can be found in several textbooks (Bushberg et al., 2002; McRobbie et al., 2005). Section 3.2 summarizes the issues concerning safety and image quality in simultaneous EEG-fMRI. Section 3.3 concentrates on image acquisition and motion compensation. Section 3.4 elaborates on how image contrast can be generated based on acquired multi-echo MRI. Section 3.5 is a short introduction to image segmentation and the C-means clustering algorithm, which is used in the BB-MRI segmentation.

3.1 MRI ACQUISITION

The atomic nucleus with a spin has a nuclear magnetic moment. If placed in a magnetic field $\boldsymbol{B_0}$, a fraction of the spins will align parallel to the $\boldsymbol{B_0}$ field and produce a net magnetization. This net magnetization can be turned with a RF field $\boldsymbol{B_1}$, which is applied perpendicular to the $\boldsymbol{B_0}$ field. For resonance to occur the $\boldsymbol{B_1}$ should be at the Larmor frequency and the frequency is determined by the local $\boldsymbol{B_0}$ (McRobbie et al., 2005, pp. 135–150). The absorbed energy will be emitted as RF signal and this signal is measured with receiver coils. The localization of the signal is performed with magnetic gradients, which are created by altering the currents in the gradient coils. The loud acoustic noise, characteristic for MRI, is caused by mechanical vibrations of the gradient coils due to gradient switching. The gradients encode the slice, phase, and frequency (Fig. 1). The echoes are collected within a set time of echo (TE) after the RF excitation pulse into a phase-frequency encoded k-space (Fig 1). The time of repetition (TR) defines the repetition interval for the pulse sequence. The k-space is transformed into a human understandable image space by fast Fourier transform (FFT). The k-space is conjugate symmetric. Cartesian sampling of the k-space is the most common way of filling the k-space, but other ways also exist.

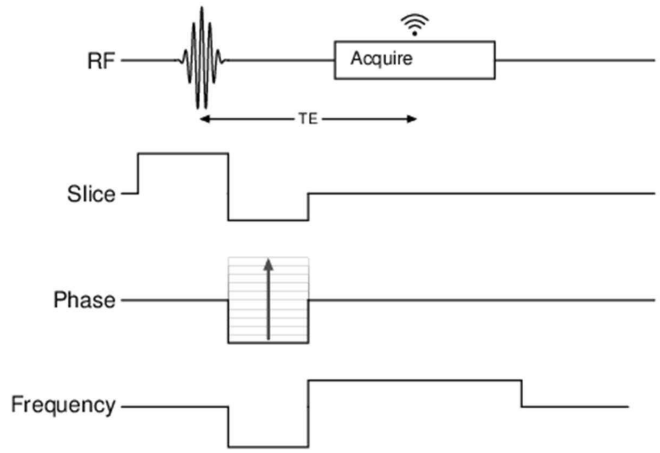

Figure 1 Sequence diagram of a GE sequence (created with the code provided by White, 2016).

Sequences are divided into two main categories: gradient echo (GE) and spin echo (SE) (McRobbie et al., 2005, p. 220). Figure 1 presents the pulse diagram for a GE sequence. In the GE sequence, the free induction decay (FID) signal is manipulated, dephasing and rephasing gradients in the frequency encoding direction. The dephasing pulse is applied immediately after the RF pulse, causing small spatial changes in resonance frequency, and leading to faster attenuation of the FID. By applying a rephasing pulse, the spins affected by the dephasing gradient will recover and the signal is collected. The signal of a standard GE sequence is defined as follows (McRobbie et al., 2005, pp. 141–146):

$$S = S_0 \, e^{-\frac{TE}{T_2^*}}, \tag{1}$$

where S_0 is the initial FID signal and T_2^* is the relaxation time. The SE sequence consists of an excitation pulse, followed by a 180º refocusing pulse. The received signal S is dependent on the composition of the tissue the following (Bushberg et al., 2002, p. 394):

$$S \propto \rho \left(1 - e^{-\frac{TR}{T_1}}\right) e^{-TE/T_2}, \tag{2}$$

where T_1 and T_2 are the respective relaxation times and ρ the proton density. The T_1 relaxation is the spin-lattice relaxation, which defines how fast the net magnetization recovers to equilibrium state. The T_2, which is the spin-spin relaxation, is a measure of the dephasing of the transverse magnetization. $\boldsymbol{B_0}$ inhomogeneity increases the dephasing and shortens the T_2 constant to T_2^* (Bushberg et al., 2002, pp. 385–387). The R_1 and R_2 values are relaxation rates and are the inverses of the T_1 and T_2 values, respectively.

3.2 SIMULTANEOUS EEG-FMRI – SAFETY AND QUALITY

MRI-compatible EEG equipment differs from regular EEG equipment. To accommodate the hardware to the MRI environment changes have been made to the equipment, including non-ferromagnetic electrodes and leads, electrode design, high input impedance of the amplifiers and material choices to reduce the effects of $\mathbf{B_0}$ field (Lemieux et al., 1997; Ullsperger & Debener, 2010, p. 76). The most substantial issue in EEG-fMRI is caused by heating due to the RF field $\boldsymbol{B_1}$ (Angelone et al., 2006; Lemieux et al., 1997). The currents induced by the gradient fields are 1/200 smaller than those induced by the $\boldsymbol{B_1}$ (Lemieux et al., 1997).

The RF exposure is noted as the specific absorption rate (SAR) and measured as watts per kilogram tissue (McRobbie et al., 2005, p. 190). The SAR estimates on the scanners are based on simulation and do not account for non-biological foreign objects (Shellock, 2001, pp. 75–95) and are calculated as follows (Jin, 1998; Yeung et al., 2002):

$$SAR = 0.5\sigma\frac{E}{\rho}, \quad (3)$$

where σ is the electrical conductivity of the tissue, ρ the tissue density, and E the root mean square of the electric field. The SAR for a conducting loop with the radius r as follows (McRobbie et al., 2005, p. 190):

$$SAR \propto \sigma r^2 \alpha^2 B_0^2 D, \quad (4)$$

where α is the flip angle and D the duty cycle. The α is determined by how long the RF field is switched on, as follows:

$$\alpha = \gamma B_1 t_p, \quad (5)$$

where γ is the gyromagnetic ratio and t_p the duration of the pulse (McRobbie et al., 2005, p. 190).

The SAR levels used are regulated by the International Electrochemical Commission in the IEC 60601-2-23 standard (International Electrochemical Commission, 2010). According to the IEC 60601-1 standard, the temperature of an object in skin contact, may not exceed 43ºC (International Electrotechnical Commission, 2005). The EEG equipment manufactures may also give guidelines. In Study **I**, Brain Product's EEG-equipment was used, and they have stated in their guidelines that the stable temperature plateau of the electrode should not exceed 45 ºC (Carmichael et al., 2010)

The heating effect has been studied with simulations and temperature measurements (Angelone et al., 2004, 2006; Carmichael et al., 2010; Lazeyras et al., 2001; Lemieux et al., 1997; Mullinger, Brookes, et al., 2008; Negishi et al., 2008; Nöth et al., 2012). The measured temperature has been observed to be linearly dependent on the SAR (Lazeyras et al., 2001; Lemieux et al., 1997), where low SAR sequences are considered safe and high SAR sequences have resulted in significant temperature increases (Meriläinen, 2002; Nöth et al., 2012).

In several studies, the EEG equipment has been noted to cause only superficial artifacts in the fMRI sequence (Bonmassar et al., 2001; Krakow et al., 2000; Mullinger, Debener, et al., 2008), which is a GE echo planar imaging (EPI) sequence. The artifacts are produced by the conductive material causing deviations in susceptibility and disturbing the $\boldsymbol{B_0}$ field (Krakow et al., 2000; Mullinger, Debener, et al., 2008). The EEG equipment should not affect the stability in the GE EPI sequence (Mullinger, Debener, et al., 2008) or in the fMRI activations (Bonmassar et al., 2001; Vasios et al., 2006).

3.3 ACQUISITION OPTIMIZATION

The image acquisition is optimized with respect to the resolution, SNR, and scan time. The image contrast is also an important aspect of optimization, which is dependent on the sequence type and its parameters.

The **resolution** defines how small details can be discerned and is determined by clinical needs.

The **SNR** is dependent on the imaging parameter and tissue consistency as follows (Bushberg et al., 2002, pp. 394, 440):

$$SNR \propto S * V * \frac{\sqrt{NEX}}{BW}, \quad (6)$$

where S is the tissue consistency-dependent signal (Eq. 1 and 2), V the volume of the voxel, NEX the number of excitations, and BW the bandwidth. The SNR is also dependent on technical aspects of the equipment such as the receiver coil, reconstruction algorithm and field strength (Bushberg et al., 2002, p. 440).

The **scan time** is, among other things, defined by the TR, matrix size and NEX. The scan time can be reduced by either acquiring less data points in k-space or sampling multiple data points during one excitation. The Partial Fourier (PF) technique utilizes the conjugate symmetry of the k-space, which reduces the size of acquisition matrix. With the PF technique, only a predefined portion of the k-space is acquired. This is possible due to the conjugate symmetry of the k-space. The reduction in scan time

with PF, will reduce the SNR since less sampling points in the k-space are acquired (McRobbie et al., 2005, p. 132). In quantitative imaging, it is important to ensure that the imaging acceleration method does not affect the quantitative values e.g. adequate SNR or spatially varying signal or noise behavior.

Managing **artifacts** is also a part of the image optimization process. Artifacts include chemical shift artifact, partial volume effects, Gibbs truncation, and motion artifacts are commonly present in MRI images (Bushberg et al., 2002, pp. 447–457). Cartesian sampling of the k-space is susceptible to motion because the frequency- and phase-encoding directions are unique. The artifacts due to motion, i.e. ghosting or blurring, are mainly produced in the phase encoding direction because these points are sampled more sparsely than the points in the frequency encoding direction. The acquisition of the adjacent time points in the phase encoding direction can have a time difference in the time scale of TR, whereas the adjacent time points in the frequency encoding direction are acquired within milliseconds. The magnitude of the ghosting artifact is dependent on the severity of the motion.

The type of the motion impacts the appearance of the artifact, for example, periodic pulsation or regular breathing can cause a few ghosts, but irregular gross patient movement or peristalsis causes overall blurring of the images (Bushberg et al., 2002, pp. 451–453; McRobbie et al., 2005, pp. 78–79). Periodic physiological movement, such as breathing or cardiac motion, can be tackled with gating or navigation echoes, where the motion is tracked and images are acquired in the same phase of the motion or data in the wrong phase are discarded (McRobbie et al., 2005, pp. 77–79). Navigator echoes can also be used to realign the images (Ehman & Felmlee, 1989). To compensate for irregular movement, one option is to collect multiple excitations and average it or sample the k-space radially. In radial sampling, the center of the k-space reduced the motion artifact in the same way as averaging. With the technique called periodically rotated overlapping parallel lines with enhanced reconstruction (PROPELLER), the center of the k-space is sampled frequently and can also be used in the same way as the navigator echo (Pipe, 1999). Gradient echo sequences can use the "stack-of-stars" k-space sampling, where the in-plane trajectory in k-space consists of radial spokes. The slice direction is sampled conventionally (Chandarana et al., 2011).

When imaging children, motion can also be reduced by using sequences with lower acoustic noise levels (Zhu et al., 2020). At our hospital, neonatal MRI is performed in the subject's natural sleep, i.e. the subject is fed and wrapped tightly and hopefully the infant has fallen asleep. The loud noise, due to gradient switching, might wake up the subject. Lower sound levels can be reached by altering the trajectory in the k-space or reducing the slew rate (Shellock & Bradley, 2000, p. 128). This might come at a cost, where the imaging times increase or SNR decreases (Alibek et al., 2014; Heismann et al., 2015). The Siemens stack-of-star sequence, called the StarVibe, has the properties of low acoustic noise and motion compensation, and was employed in Study **IV** for BB-MRI.

3.4 DERIVED IMAGE CONTRASTS

The image contrast and SNR are based on the sequence type and mainly its TE and TR values and, of course, on the tissue consistency (Eq. 1 and Eq. 2).

In RT planning, in-phase (IP) and out-of-phase imaging (OOP) is often used, i.e. the Dixon method (Dixon, 1984). The Dixon method utilizes the small difference in the resonance frequency of the water and fat. The IP images are acquired with a TE when the water and fat are in the same phase. The OOP images are acquired with a TE when the water and fat are out-of-phase. From the acquired IP and OOP images, it is possible to calculate the water- and fat-only images (McRobbie et al., 2005, p. 90):

$$(7) \qquad Water\ only\ image = \frac{IP+OOP}{2},$$

$$(8) \qquad Fat\ only\ image = \frac{\mathrm{IP}-}{2},$$

In this thesis, the IP and fat-only images were used in the segmentation for BB-MRI images (Studies **III** and **IV**).

The GEPCI post-processing technique (Study **V**) is described in detail e.g. Luo et al. (2012). The image reconstruction begins from raw data consisting of complex data from each channel separately. These images are combined by the method developed by Quirk (2009), which enables optimal estimation of quantitative parameters, i.e. the decay rate R_2^*. Before the signal fitting, the phase data must be unwrapped in the time domain and partly in the space domain. From the combined images $S(TE_n)$, the generated image contrasts are based on estimating the S_0 (i.e. T_1 image), the R_2^*, and the frequency map f by assuming mono-exponential signal decay (Luo et al., 2012):

$$(9) \qquad S(TE_n) = S_0^2 * e^{-R_2^*(TE_n - T_1)} * e^{i2\pi f(TE_n - TE_1)},$$

where TE_n is the TE time of the image. In this thesis, only T_2^* values are of interest in Study **V**, and the generation of other image contrasts will be presented as a curiosity only. The frequency map f, obtained from signal fitting to Equation 9, is high pass filtered and rescaled. This will create the frequency map (FM) The GEPCI-SWI images can, for instance, be created as follows (Luo et al., 2014):

$$(10) \qquad S_{GEPCI-SWI}(TE) = e^{-R_2^* * TE} * FM^4,$$

The calculation of other image contrast can be found in Luo et al. (2012).

3.5 IMAGE SEGMENTATION WITH FUZZY C-MEANS CLUSTERING

The aim of the image segmentation is to classify tissue into separate categories. This can, for instance, be used to estimate volume properties or render 3D visualizations. The simplest way of carrying out segmentation is thresholding, where classification is based on image intensity (Toennies, 2017, p. 226). This requires that the intensities be homogeneous across the image, which is the case when creating 3D visualization from CT images (Vannier et al., 1989) used for craniosynostosis diagnostics. In MRI images, there is a bias field present. The bias field is a low frequency spatial intensity change and results in different intensities of the same tissue within an image volume. In MRI, the bias field is caused by spatially varying coil sensitivity (Collins & Smith, 2001) and subject motion (Sled & Bruce Pike, 1998). The estimation of the bias field must be data-specific because the bias field is patient- and sequence-dependent (Ahmed et al., 2002).

Image clustering algorithms classify voxels based on intensity value and their surroundings. In fuzzy clustering, a voxel can belong to multiple classes and results in probability values of the voxel belonging to cluster *c*. Fuzzy c-means clustering was originally developed by Dunn (1973) and enhanced by Bezdek (1984), where the aim was to minimize a function J_m. Ahmed et al (2002) proposed a modification, by adding the latter term in the following Equation 11 to take into account the labeling of the neighborhood N_k:

$$J_m = \sum_{i=1}^{c} \sum_{k=1}^{N} u_{ik}^{p} \|x_k - v_i\|^2 + \frac{\alpha_w}{N_R} \sum_{i=1}^{c} \sum_{k=1}^{N} u_{ik}^{p} \left(\sum_{x_r \in N_k} \|x_r - v_i\|^2 \right), \tag{11}$$

where x_k is the observed value of the voxel, N_R the cardinality of N_k, α_w the weighting factor for the neighborhood, p the weighting exponent determining the fuzziness of the classification, u_{ik} the partition matrix, and v_i the cluster prototypes (Bezdek et al., 1984).

In the bias field corrected fuzzy c-means clustering (BCFCM), algorithm the bias field β_k in voxel k is simply assumed to be additive (Ahmed et al., 2002)

$$y_k = x_k + \beta_k \tag{12}$$

where y_k and x_k are the actual and observed log-transformed intensities in the voxel k, respectively. By substituting Equation 12 to Equation 11, the minimization function is given the following form (Ahmed et al., 2002):

$$(13) \qquad J_m = \sum_{i=1}^{c}\sum_{k=1}^{N} u_{ik}^{p}\|y_k - \beta - v_i\|^2 + \frac{\alpha_w}{N_R}\sum_{i=1}^{c}\sum_{k=1}^{N} u_{ik}^{p}\left(\sum_{x_{r\in N_k}}\|y_r - \beta - v_i\|^2\right)$$

The minimization of the function J_m. can be solved using a Lagrange multiplier and the derivation of the Lagrangian multiplier with respect to u_i, v_i and β_k.. This will result in a partition matrix (Ahmed et al., 2002)

$$(14) \qquad u_{ik} = \left(\sum_{j=1}^{c}\left(\frac{\|y_k-\beta_k-v_i\|+\frac{\alpha_w}{N_R}\sum_{x_{r\in N_k}}\|y_r-\beta_r-v_i\|}{\|y_k-\beta_k-v_j\|++\frac{\alpha_w}{N_R}\sum_{x_{r\in N_k}}\|y_r-\beta_r-v_j\|}\right)^{\frac{1}{p-1}}\right)^{-1},$$

cluster prototypes (Ahmed et al., 2002)

$$(15) \qquad v_i^* = \frac{\sum_{k=1}^{N}(\hat{u}_{ik})^m\left((y_k-\beta_k)+\frac{\alpha_w}{N_R}\sum_{x_{r\in N_k}}(y_r-\beta_r)\right)}{(1-\alpha_w)\sum_{k=1}^{N}(\hat{u}_{ik})^m},$$

and a bias field estimator (Ahmed et al., 2002)

$$(16) \qquad \beta_k = y_k - \frac{\sum_{i=1}^{c} u_{ik}^{p} v_i}{\sum_{i=1}^{c} u_{ik}^{p}},$$

Basically, after the initialization of the initial cluster values v_i, the BCFCM algorithm will iterate by updating first the partition matrix (Eq. 14), then calculating the cluster prototypes (Eq. 15), and finally estimating the bias field (Eq. 16). This will repeat until a preset termination criterion is met.

4 MATERIALS AND METHODS

All studies were approved by the Ethics Committee of the Hospital District of Helsinki and Uusimaa and a written informed consent was obtained from all subjects or their legal guardians.

4.1 SIMULTANEOUS EEG-FMRI – SAFETY AND QUALITY

4.1.1 TEMPERATURE MEASUREMENTS

The motivation for Study **I** was to assess the safety of the EEG equipment for sequences other than those approved by the manufacturer. The sequences were chosen from the hospital's clinical epilepsy and/or fMRI protocols because these are more likely to be needed in clinical settings.

The phantom measurements were carried out on two 3 T scanners: Philips Achieva (Philips Medical Systems, Best, the Netherlands) and Siemens Verio (Siemens, Erlangen, Germany). The volunteer studies were performed only with the Philips scanner. The following sequences were used: GE EPI, T_1-weighted 3D (T1 3D), T_1-weighted inversion recovery (T1 IR), ME GE for B_0 correction, diffusion MRI (dMRI), and T_2-weighted TSE (T2 TSE) sequence.

EEG caps manufactured by Brain Products (Brain Products, Munich, Germany) were used in all phantom studies and the three volunteer studies. The electrode configuration and cap model varied. The size 56 and 60 had 64 electrodes, whereas the size 52 cap had only 32 electrodes. Some of the most frequently used caps had to be renewed in 2011. The new caps had electrodes with a smaller contact surface than the older ones purchased in 2005 (Fig. 2) and a pin sensor design, reducing the amount of Ag/AgCl in the cap (Brain Products, 2008). The volunteer studies were conducted with the caps of size 56 and 60 caps purchased in 2005. ECI electrogel (Electro-Cap International, Inc, Eaton, OH, USA) paste was used in some of the measurements.

For these measurements, an MRI-compatible 8-channel FISO TMI (FISO Technologies, Sainte Foy, Quebec, Canada) temperature meter was used. The aim was to measure the temperature of a sufficient sample of the electrodes, because according to a previously reported simulation study no singular hot spots can occur in a 3 T environment (Angelone et al., 2004).

In total, 20 volunteer and 30 patient studies were performed, where simultaneous EEG-fMRI data were collected.

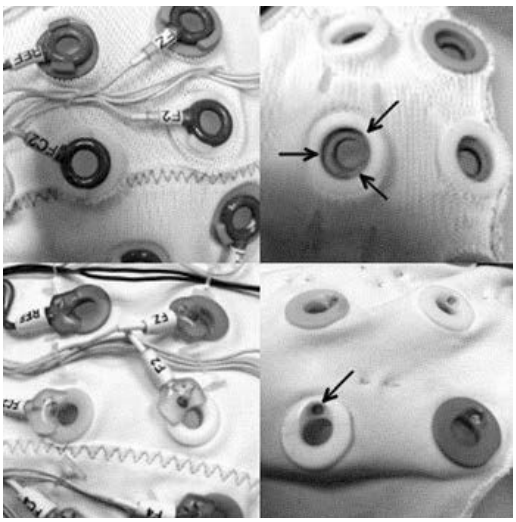

Figure 2 Electrode design of the caps. The top row shows the electrodes of the EEG caps purchased in 2005, with a large contact surface. The bottom row shows the electrodes of the EEG caps purchased in 2011. Arrows indicate the location of the contact surface.

4.1.2 IMAGE QUALITY IN SIMULTANEOUS EEG-FMRI

The phantom used in Study **II** was constructed according to the instructions of Friedman and Glover (2006), and the measurements were carried out on two 3 T from different vendors. On both scanners, there were two imaging sessions and each session consisted of four fMRI acquisitions. Between each acquisition, the phantom was repositioned. With a few modifications, the quality assurance fMRI sequence published by Biomedical Informatics Research Network (fBIRN) was used. In the image quality measurements, the impact of the EEG equipment on the temporal stability, SNR, and extent of artifacts was assessed.

The study also included a retrospective assessment of human fMRI data acquired from two volunteers, where one of the volunteers was imaged twice. A region of interest (ROI) -based assessment of the functional data (Simmons et al., 1999) was conducted on both phantom and volunteer data.

To assess the impact of EEG equipment on the image quality of anatomical images, an example of an image artifact observed in one volunteer study in the simultaneous EEG-fMRI project was included in this thesis.

4.2 CRANIOSYNOSTOSIS IMAGING WITH MRI

Study **III** presents the segmentation algorithm and the initial results. Study **IV** evaluated the MRI segmentations in comparison with the CT images. Acquisition and post-processing optimization were performed to ease the clinical use of the BB-MRI. The main emphasis was on the post-processing, with the aim of fully automizing the segmentation process.

Patients aged 3 months to 8 years were imaged for diagnostic purposes. The BB-MRI sequence was imaged in addition to the normal clinical imaging protocol. In Study **III,** two 3T Siemens scanners were used: Verio and Skyra (Siemens Healthcare, Erlangen, Germany). In Study **IV,** the data were acquired only with the Siemens Skyra scanner. All imaging was performed with a 32-channel head coil. The BB-MRI sequence was based on the original work by Eley et al. (Eley et al., 2013, 2014; Eley, McIntyre, et al., 2012; Eley, Watt-Smith, et al., 2012), and the sequence used was a Volumetric Interpolated Breath-hold Examination (VIBE) sequence. The sequence is a variant of the spoiled 3D GE sequence, where zero-filling in k-space is used. In RT, Dixon imaging is used for construction of synthetic CT for dose planning (Berker et al., 2012; Korhonen et al., 2014; Wang et al., 2017), and thus, acquisition of OOP was later incorporated.

As interest in imaging infants with the BB-MRI sequence arose, there was a need for a sequence with lower acoustic noise levels and that was less susceptible to motion. The GE sequence has a high acoustic noise level (Shellock & Bradley, 2000, p. 128) and the 3D acquisition is highly susceptible to motion (Bushberg et al., 2002, p. 439). Thus, in Study **IV** three patients were imaged with the Siemens implementation of the 3D stack-of-star sequence, i.e. the StarVibe sequence, which has lower acoustic noise levels and is less sensitive to movement than the VIBE sequence.

The initial segmentation testing was performed on tools included in the 3D Slicer software (Fedorov et al., 2012). In general, the segmentation failed because of the bias field in the images. The availability of the 3D bias field corrected fuzzy c-means clustering (BCFCM) (Ahmed et al., 2002) as implemented in Kroon (2020) and giving promising results in preliminary testing, led to scripting the processing pipeline on Matlab® (MathWorks Inc., Natick, Massachusetts, USA) platform. The flowchart of the processing steps is presented in Figure 3.

The reorientation of the images was performed with FMRIB Software Library (FSL) (Smith et al., 2004; Woolrich et al., 2009), but otherwise Matlab functions were used in the preprocessing stage. For the skull segmentation of the IP images, the mean intensity of the skull was calculated from a coarse slice-by-slice Otsu thresholding segmentation. The mean intensity from the background was also estimated from the IP image. The fat-only images were calculated according to Equation 8 and segmented into two categories (background and fat), where the initial values for the background mean and half of the maximum intensity of the fat-only image were used.

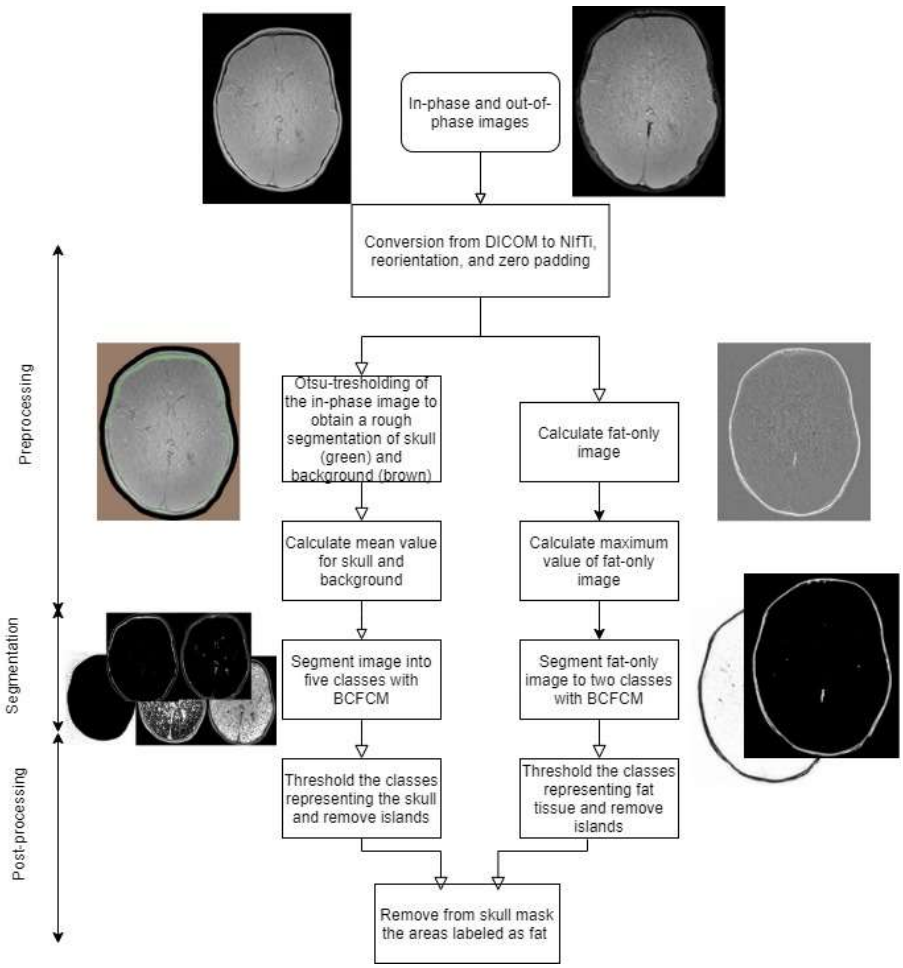

Figure 3 Flowchart of the segmentation

The BCFCM algorithm was used as is and it was tested with segmentation to three, four and five categories. The output of the BCFCM algorithm is the probability of the voxel belonging to a category, and therefore, different thresholds were tested for each category. The changes made to the sequence were based on the post-processing requirements. The sequence optimization was tested for the impact of BW, slice orientation (transversal and sagittal plane), resolution, PF in slice direction, and flip angle. Typically, two BB-MRI sequences were acquired in an imaging session, with the first one being the best sequence and the latter one being the modified test sequence. The same test sequence was acquired from at least two patients. The image quality and the output of the segmentation algorithm were compared for two sequences. The sequence with a better segmentation output was used thereafter. After

adding the OOP acquisition, also segmentation of the water-only images (Eq. 7) was evaluated for a few patients. All segmentations were evaluated visually.

Study **IV** compared the current gold standard modality CT with the proposed BB-MRI method. At an early stage of the research project, BB-MRI was considered sufficiently reliable,and therefore, CT images were not acquired. Thus, comparison of ground truth acquired with CT was available for only nine patients. The assessment was made by two experienced neuroradiologists, two craniofacial surgeons and one pediatric neurosurgeon. The statistical analysis was carried out on Microsoft Excel (Microsoft) and SPSS statistics software (IBM) version 24. Krippendorff's alpha statistics was used to assess the inter-rater reliability of the five raters. They evaluated the appearance of the sutures and intracranial impression. The neuroradiologist carried out the rating twice, which enabled assesment of intra-rater reliability was calculated by both percentage agreement and Cohen's κ statistics between ratings.

4.3 MULTI-CONTRAST IMAGING WITH GRADIENT ECHO PLURAL CONTRAST IMAGING

The GEPCI sequence is a 3D spoiled GE sequence with ten TEs, a resolution of 1x1x2 mm^3, and whole brain coverage. The main issue with the GEPCI sequence was the relatively long imaging time of approximately12 minutes in a clinical setting. To assure the comparability to previously collected data, the sequence parameters were held as close as possible to the parameters presented in the article by Luo et al. (2012) and no compromise in the current resolution was accepted. Thus, the only possibility was to reduce scan time by applying imaging acceleration techniques. The PF method was considered to be the most promising imaging acceleration technique because it does not cause spatially dependent intensity behavior in either signal or noise.

The study consisted of phantom, volunteer, and patient image acquisitions. All data were acquired on a 3T Siemens Verio (Siemens Healthcare, Erlangen, Germany) with GEPCI sequence with α 30º, TR 49 ms, TE 4-40 ms, anda ΔTE 4 ms.

The phantom measurements were performed to assess the feasibility of using the PF acquisition as an imaging acceleration technique. The phantom measurements were carried out using a phantom by the American College of Radiology (ACR) and a 12-channel head coil. The phantom was imaged with the slice thickness of the original GEPCI sequence (2 mm) as well as with 5 mm slice thickness. Images were acquired with the original sequence and with sequences using PF in phase (PFP) or slice (PFS) encoding direction. On the Siemens scanner, both PFP and PFS had two possible values 6/8 and 7/8 of the k-space. In addition, data with the combination of PFP and PFS were acquired. This resulted in nine measurement for each slice thickness. For further investigations, two volunteers were imaged on the same scanner to evaluate

the imaging acceleration techniques. One volunteer was imaged with a 12-channel and the other with a32-channel head coil.

The post-processing of raw data was performed with an in-house program with MATLAB. Data were exported from the scanner with the Siemens TWIX application because the scanner was unable to reconstruct the images for each coil element separately. The TWIX k-space data were read with MATLAB functions by Philipp Ehses (Parker et al., 2014), and these data were then reconstructed to the image space with 3D FFT. Coil-channel combination was done with a sum-of-squares method, where phase offset was eliminated by setting phase to zero at the first TE in every channel. The fitting was performed by the least square method to the mono-exponential decay in Equation 9.

Image quality assessment of the ACR phantom was performed with an in-house MATLAB program (Mäkelä et al., 2012) according to the phantom vendor instructions (American College of Radiology, 2005). The assessment was made from the first magnitude images of the first TE and included estimation of percentage integral uniformity (%), slice thickness accuracy, and low-contrast object detectability and SNR.

The impact of PF on the T_2* values was assessed in two different ways: an overall median value and a voxel-wise median difference. The voxel-wise median differences of T_2* values were calculated as in Ruuth (2019):

$$\Delta T_2^* = T_{2,original}^* - T_{2,PF}^* , \tag{17}$$

where T_2* values indicate either the original data or the one where PF is used.

5 RESULTS

The results for Studies **I** and **II** are presented in Section 5.1, those for Studies **III** and **IV** in Section 5.2, and those for Study **V** Section 5.3.

5.1 SIMULTANEOUS EEG-FMRI

The assessment of simultaneous EEG-fMRI consisted of two parts: safety (Study **I**) and impact of EEG equipment on image quality (Study **II**).

5.1.1 SAFETY OF SIMULTANEOUS EEG-FMRI

In total, eight phantom and three volunteer measurements were conducted in Study **I**. In the phantom measurements the observed overall highest temperature increase was 4.1ºC with the T2 TSE sequence (Table 1), which had the highest SAR (Fig. 4). Higher temperature increases were observed with the older cap model (2005) than with the newer ones from 2011 (Table 1).

Table 1. *Mean and maximum temperature changes measured with the Philips and Siemens scanner for the T2-TSE sequence.* (Kuusela et al., 2015) *Reprinted with permission from SAGE Publications*

Measurement	Scanner	Purchase year	Cap size	Electrode gel applied	Nbr of electrodes measured	Scan time (min:sec)	Mean $\Delta T^{\dagger}$ *(°C)	Max. $\Delta T^{\dagger\dagger}$ (°C)	Electrode with max. ΔT
P1	Philips	2005	**52**	Yes	33	5:14	0,7 ± 0,7	3,7	O1
P2	Philips	2005	56	No	26	3:40	1,2 ± 1,1	4,1	FP2
P3	Philips	2011	56	Yes	25	5:14	0,3 ± 0,2	1,0	T8
P4	Philips	2005	60	No	5	5:14	0,9 ± 0,8	2,1	T7
P5	Philips	2005	60	Yes	5	5:14	1,0 ± 1,2	3,2	T7
P6	Siemens	2005	56	Yes	12	6:40	0,4 ± 0,3	1,4	FP1
P7	Siemens	2011	56	Yes	25	6:40	0,4 ± 0,3	1,2	T8
P8	Siemens	2009	60	Yes	12	3:20	0,3 ± 0,2	0,8	FP2

† *Mean and standard deviation of the maximum temperature measured from all electrodes*
†† *Maximum temperature measured.*

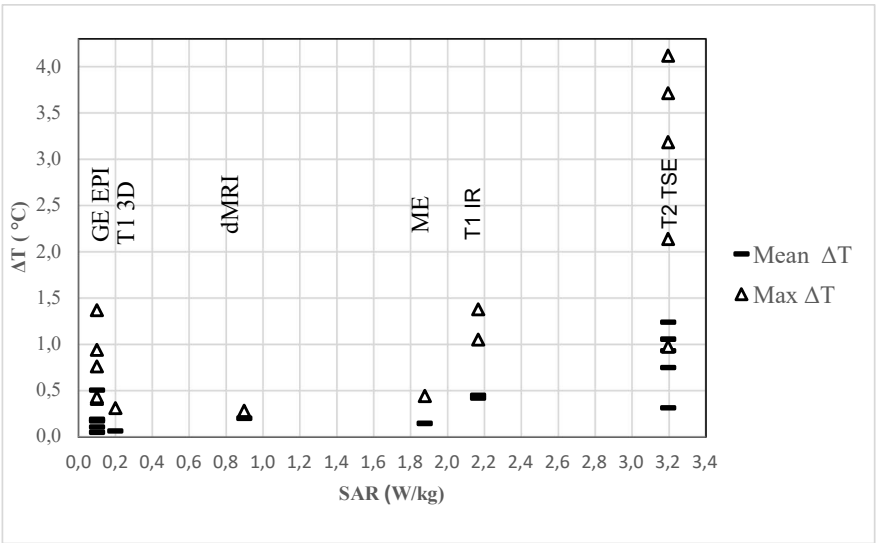

Figure 4 Mean and maximum temperature changes as a function of specific absorption rate (SAR) in the phantom measurements for the Philips scanner.

Figure 5 provides a spatial representation of the measured temperature changes for EEG cap sizes 52 and 56 purchased in 2005, i.e. the old model of the EEG cap. Figure 6 depicts the measured maximum temperature changes for EEG cap size 56 (purchased in 2011) using Philips and Siemens scanners. Accordingly, with all EEG caps the highest temperature increases were observed in the peripheral electrodes. There were no clear foci in which the large temperature increases were most likely to occur. Due to improved electrode design and reduced radius of the conductive loop for the EEG caps purchased in 2011, the temperature increases should be lower than for the caps purchased in 2005. This was verified in this study.

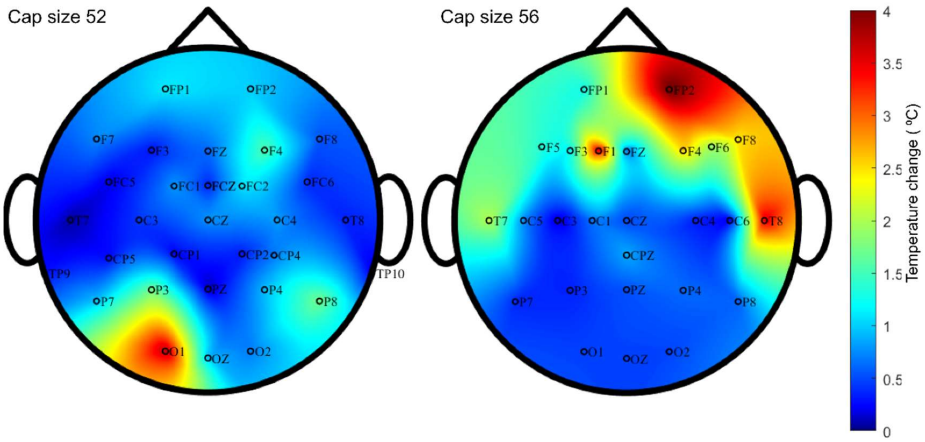

Figure 5 Visualization of the measured temperature changes (ºC) for EEG cap size 52 purchased in 2005 on the left and cap size 56 on the right. Only the locations of the measured electrodes are shown. Figure created with a code by Martinez-Cagigal (2019)

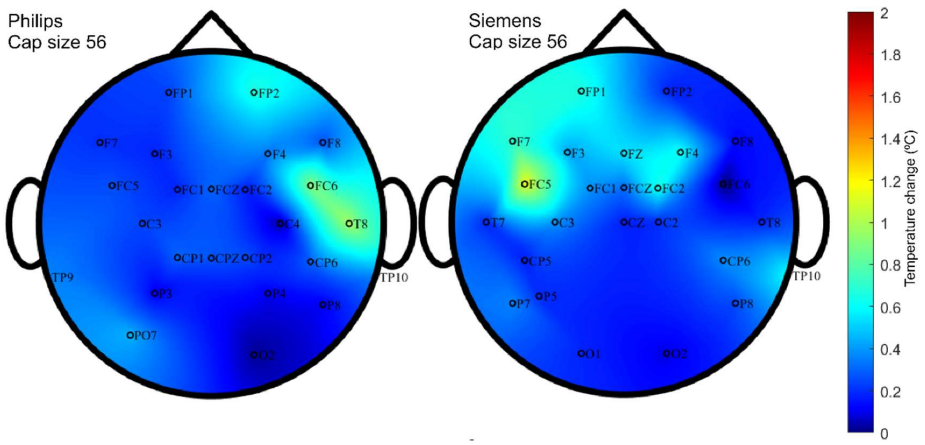

Figure 6 Visualization of the measured temperature changes (ºC) for EEG cap size 56 purchased in 2011 using the Philips scanner on the left and the Siemens scanner on the right. Only the locations of the measured electrodes are shown. Note that the scaling differs from the scaling in Figure 5. Figure created with a code by Martinez-Cagigal (2019)

In the volunteer studies the highest temperature increase was 2.1ºC for the T2 TSE sequence, which is consistent with the phantom measurements. None of the volunteers reported any sensation of heating of the electrodes.

5.1.2 IMAGE QUALITY IN SIMULTANEOUS EEG-FMRI

In the phantom studies (Study **II),** the artifacts caused by the EEG cap in the GE EPI images were superficial. The average artifact depth was 12-15 mm. For the ECG and EOG, the artifact extended up to 50 mm. In the volunteer studies, the artifacts did not affect the image quality in brain tissue. Based on the ROI analysis, the average SNR reduction was 15% and 18-30% in phantom and volunteer studies, respectively.

In one volunteer study imaged for the simultaneous EEG-fMRI project, there was an artifact in the T1 IR images (Fig. 7, top row). The artifact affected the image quality by deteriorating the discernibility of the brain tissue. The artifact was not observed in other images acquired in the same session (Fig. 7, middle and bottom row) or in any other volunteers.

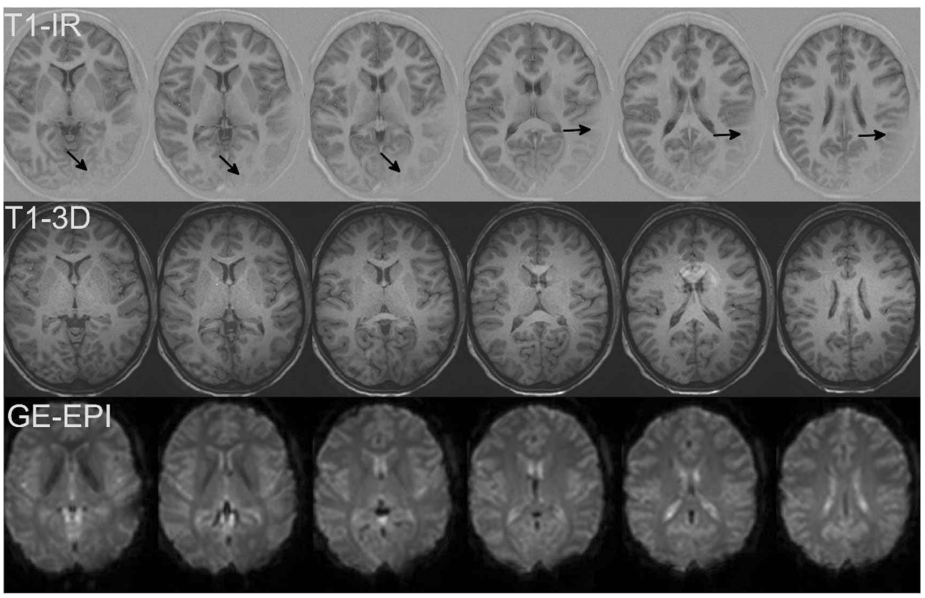

Figure 7 Top row: the artifact observed in one of the volunteer studies. Bottom row: T13D acquired in the same imaging session. Arrows indicate the location of the artifact.

5.2 CRANIOSYNOSTOSIS IMAGING WITH MRI

Study **III** assessed the usability of the BB-MRI method in children with posterior plagiocephaly and presented a semi-automatic BB-MRI segmentation workflow (Fig. 3). Posterior plagiocephaly was observed in all 15 patients.

For Siemens Skyra, the BB-MRI sequence was finally fixed to an approximately 2-minute transversal slice orientation IP and OOP sequence with a field of view 192*168 mm, matrix size 192*162, zero-fill interpolation, slice thickness 0.9 mm, TR 8.28 ms and TE 2.46/6.15 ms, flip angle 5º, parallel imaging factor 2, and BW of 810 Hz/pixel.

Figure 8 presents 3D rendered images from different types of segmentations: IP images only, IP and OOP images, the StarVibe sequence, and CT. Based on the visual evaluation of the segmentations, the final segmentation algorithm was initialized with five cluster classes for the IP images and two cluster classes for the fat-only images (Fig. 8 third row). The segmentations of water-only images were generally not as good as the segmentations of IP images because in the latter the bone was more consistently black.

By segmenting the fat-only images, it was possible to eliminate some of the misclassifications of the BCFCM algorithm. For example, in Figure 8 (top row) there is a large misclassified area in the posterior parts of the skull that is correctly classified when OOP image information is used (Fig. 8, second row). For infants in Study **IV,** a StarVibe sequence was used and the segmentation can be seen in Figure 8 (third row). The acquired voxel size is ca. 60% larger for the StarVibe sequence than for the regular BB-MRI sequence. The image contrast of the StarVibe images is also slightly different from that of the regular VIBE sequence.

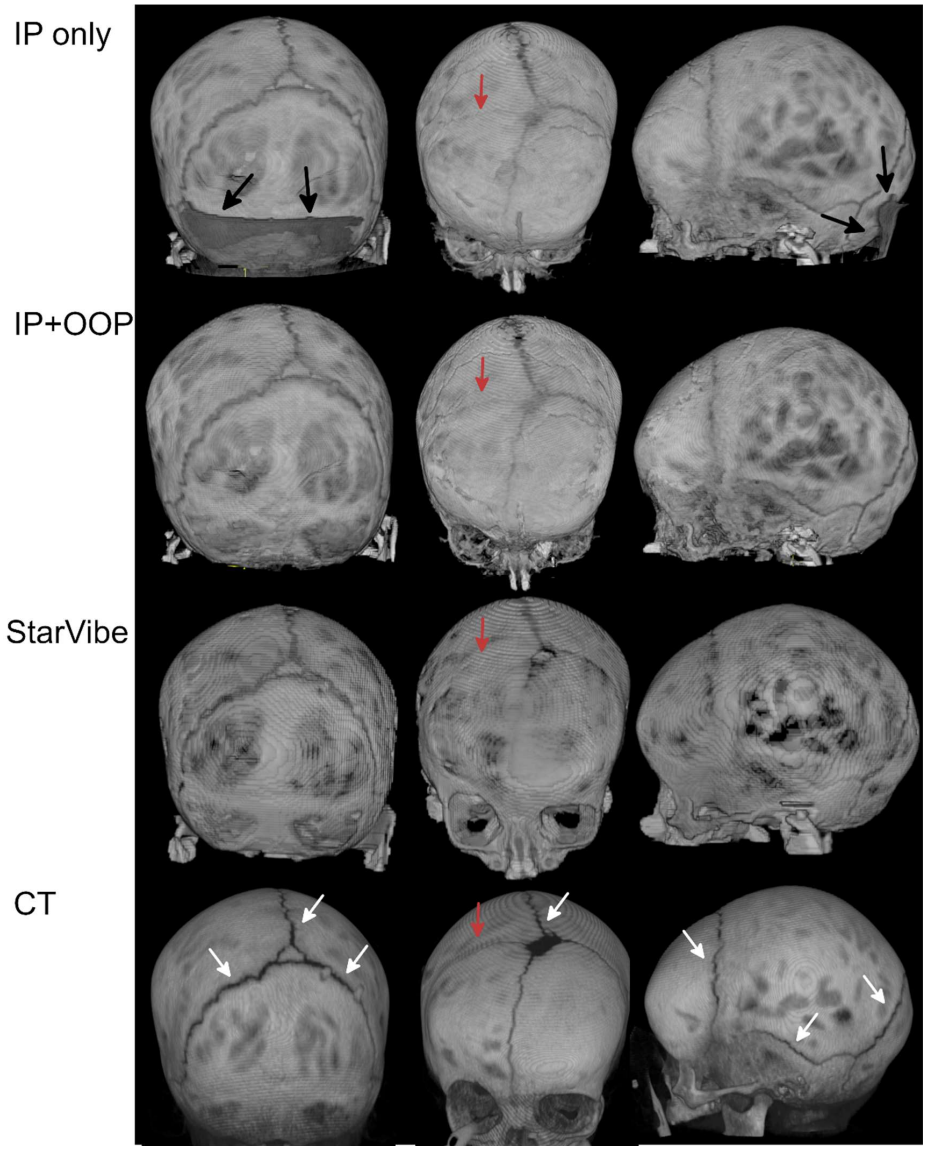

Figure 8 Example images of a 3-year-old patient of segmentations from different data in comparison to with CT. Red arrow indicate the location of closed suture. Top row: the segmentation from IP images only, where black arrows indicate artifact due to incorrect segmentation. Second row: segmentation based on IP and OOP images. Third row:segmentation based on the StarVibe sequence. Bottom row 3D renderings of CT images, where white arrows indicate the open sutures.

In addition to BB-MRI, anatomical images were acquired. Figure 9 presents the BB-MRI, CT, and anatomical images of a 6-month-old patient (Study **III**), with pathological findings in the anatomical MRI images.

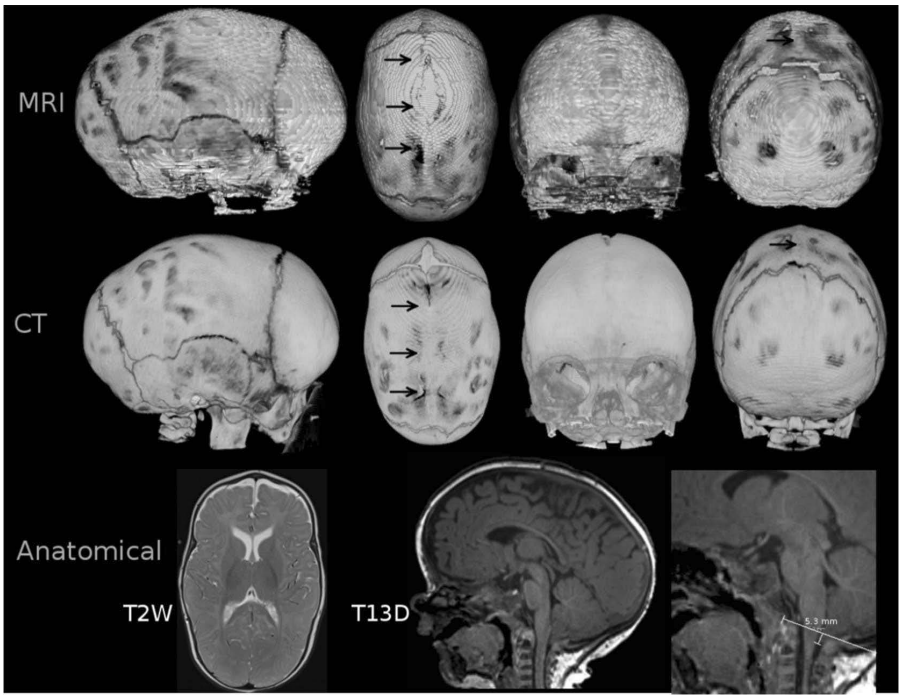

Figure 9 A 6-month-old patient with sagittal synostosis (Study **III**). Top row: 3D-rendered BB-MRI images. Middle row: 3D rendered CT images. Arrows points at the closed suture. Bottom row: anatomical T2W and T13D images. In the T2 images minor left cerebellar hemisphere hemorrhage was observed (not shown) and in the T13D images Chiari malformation was observed. (Printed on permission of © Springer-Verlag GmbH Germany, part of Springer Nature 2018)

Study **IV** assessed concordance of BB-MRI and CT, and with both modalities the diagnosis of craniosynostosis was made for all 9 patients. For sutures, the inter-rater reliability of Krippendorff's alpha was 0.953 and 0.950 for CT and BB-MRI, respectively. For older patients, the visualization of bony structures was considered more accurate. In assessing the sutures, the intra-rater reliability of the neuroradiologist was high. When assessing the intracranial impressions, the inter-rater reliability was low with both modalities, with Krippendorff's alpha being 0.553 and 0.458 for CT and BB-MRI, respectively. The intracranial impressions were assessed as more severe in BB-MRI images than in CT images.

5.3 MULTI-CONTRAST IMAGING WITH GRADIENT ECHO PLURAL CONTRAST IMAGING

Study **V** results of the phantom measurements are presented in Table 2. An increase in slice thickness was observed with use of PFS, especially with the 5 mm slice thickness.

Table 2. *Results off phantom measurements in Study **V*** (Ruuth et al., 2019). *Table reprinted with permission from Elsevier.*

Slice thickness (mm)	Parameters	Median T2* (ms)	Median ΔT2* (ms)	SNR	Slice thickness (mm).	Contrast (40)	Scan time (min:s)
2	Original	119	-	37,8	2,8	37	14.08.00
	$PFP_{7/8}$	121	2,1	38,7	2,8	39	12:22
	$PFS_{7/8}$	120	1,1	38,0	3,1	38	12:22
	$PFP_{6/8}$	120	0,7	38,5	2,7	39	10:37
	$PFS_{6/8}$	119	0,1	36,3	3,5	33	10:37
	$PFP_{7/8}$ + $PF_{S7/8}$	119	0,6	36,3	3,1	37	10:50
	$PFP_{7/8}$ + $PFS_{6/8}$	119	0,4	36,4	3,6	31	9:17
	$PFP_{6/8}$ + $PFS_{7/8}$	122	3,0	36,3	3,1	39	9:17
	$PFP_{6/8}$ + $PFS_{6/8}$	118	-0,03	36,3	3,1	39	7:58
5	Original	131	-	20,5	4,9	29	
	$PFP_{7/8}$	131	-0,4	20,9	5,3	26	
	$PFS_{7/8}$	145	11,3	21,3	5,8	15	
	$PFP_{6/8}$	131	-0,7	20,9	5,4	30	
	$PFS_{6/8}$	105	-23,4	20,7	6,2	7	
	$PFP_{7/8}$ + $PF_{S7/8}$	145	10,2	21,1	5,4	18	
	$PFP_{7/8}$ + $PFS_{6/8}$	106	-23,1	20,7	6,2	8	
	$PFP_{6/8}$ + $PFS_{7/8}$	146	11,6	21,3	5,7	26	
	$PFP_{6/8}$ + $PFS_{6/8}$	106	-22,6	20,7	6	13	

Based on phantom measurement results, the combination of the PFP and PFS was not investigated further in the volunteer studies. The impact of PF technique on the T_2* values in the volunteer studies is presented in Figure 10.

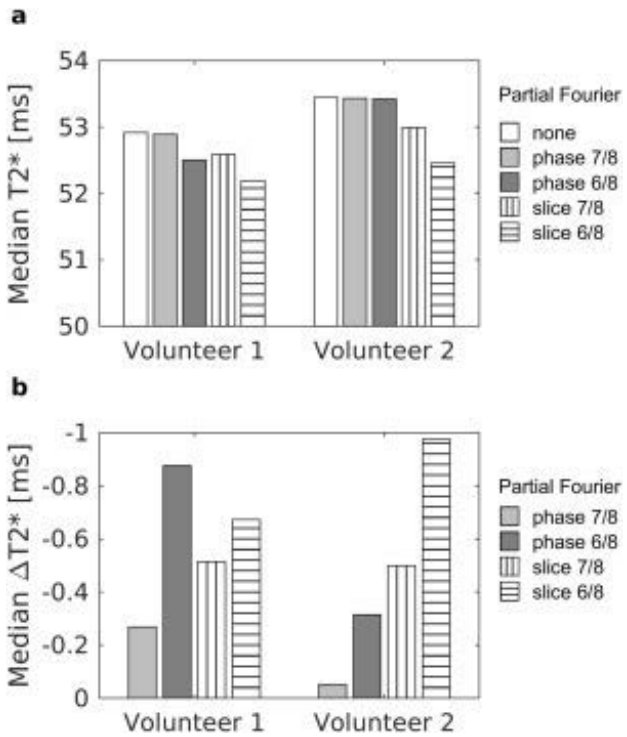

Figure 10 (a) Median T_2* and (b) voxel-wise ΔT_2* of two healthy volunteers imaged with different Partial Fourier settings. Volunteer 1 was imaged with a 12-channel head coil and volunteer 2 with a 32-channel head coil (Ruuth et al., 2019). Reprinted with permission from Elsevier.

6 DISCUSSION

This section is divided into three subsections. Section 6.1 discusses the results of Studies **I** and **II,**Section 6.2 results of Studies **III** and **IV,** and the final section 6.3 the results of Study **V**.

6.1 SIMULTANEOUS EEG-FMRI

In Study **I**, the maximum temperature increase observed was 4.1ºC and 2.1ºC in phantom and volunteer studies, respectively. The temperature increases were considered acceptable and did not exceed the maximum temperature limits set by the manufacturer of the EEG equipment. Thus, the protocol can be expanded to include the sequences measured. However, this applies to the specific setup used in Study **I,** and care should be taken if the equipment changes or is modified. The volunteer studies were performed only with the caps purchased in 2005. Based on the phantom measurements, less heating should occur for the caps purchased in 2011.

According to the studies by Angelone et al. (2004, 2006), the highest temperature increases should be observed at the CPZ electrode and without electrode paste. For high SAR sequences the overall highest temperatures were observed at the peripheral electrodes when EEG paste was used (Fig. 5). The EEG paste conducts also heat, thus, the measurements with EEG paste present may be more forgiving of the misplacement of the temperature sensor. A simultaneous EEG-fMRI study should always be conducted with electrode paste to minimize the impedance between skin and electrode (Partanen & Cheour, 2006, pp. 65–66), but the contact may inadvertently deteriorate or break off completely during the study.

The temperature increases were shown to be dependent on the SAR, but the linearity could not be verified. The SAR has been established to perform poorly in estimating the heating effect (Baker et al., 2004; Mattei et al., 2008; Nöth et al., 2012). A better way to estimate the heating is to use the $B_{1,rms}$ value, which does not make assumptions about the consistency of the subject. In addition, differences exists in how manufacturers estimate the SAR and as well as in the power of the $\boldsymbol{B_1}$ field (Baker et al., 2004). However, SAR is the only value that is recorded in the DICOM headers and can be obtained retrospectively. Measuring the RF-induced heating is dependent on e.g. the positioning of the head and lead configuration (Mattei et al., 2008), which might explain the large range of results obtained.

The most challenging part of the measurements performed in Study **I** was the placement and handling of the extremely sensitive temperature sensor. For the EEG caps purchased in 2011, the contact surface of the electrodes is small and not visible from the outside (Fig. 2). In addition, the temperature sensors did not withstand

bending and broke easily. This complicated the positioning of the temperature sensors. In this study, the possible heating of the ECG electrode was overlooked, which may serve as an interesting aspect for future studies. Uji et al. (2018) observed the highest temperature increase in the ECG electrode. The ECG electrode has also caused severe burns in other MRI studies, but in these cases a MR-incompatible ECG equipment was used (Abdel-Rehim et al., 2014).

In Study **II,** a lower SNR was observed in the fMRI sequences when the EEG equipment was present. The equipment does not affect the stability. It has previously been reported that the EEG equipment causes only superficial artifacts and should not have an impact on the image quality in the brain tissue (Bonmassar et al., 2001; Krakow et al., 2000; Mullinger, Debener, et al., 2008). This was verified in Study **II**. The EOG and ECG caused an approximately three times larger artifact, but in human studies the electrodes are not located within the field of view, and thus not affecting the image quality. The severity of the artifacts and SNR reduction are dependent on the EEG cap and gel type (Bonmassar et al., 2001; Negishi et al., 2008).

In the T1 IR sequence (Fig. 7), artifacts were observed that were not visible in other sequences acquired in the same session. The artifact were not observed in any other volunteer studies. Possibly, there is a reduction in SNR that the human eye cannot discern, and the signal behavior is also sequence-dependent. If the anatomical images acquired during an EEG-fMRI study are to be used, for example, for segmentation of brain structures or tissue, one should be aware of the potentially lower SNR and thereby misclassification.

As new imaging techniques emerge and become clinical practice, it is important to evaluate the safety of these techniques with respect to the EEG equipment. For instance, simultaneous multi slice (SMS), which is used for imaging acceleration and enables simultaneous acquisition of multiple slices, is achieved by two-channel RF excitation, increasing the SAR of the sequence. However, there are different implementations of the SMS sequence and the behavior might differ (Koopmans et al., 2012; Norris et al., 2011; Wong, 2012). Image quality should also be assessed.

6.2 CRANIOSYNOSTOSIS IMAGING WITH MRI

Study **III** presents the initial segmentation algorithm, which has since evolved. Study **IV** concluded that the sutures are observed equally accurately in BB-MRI and CT. Compared with CT, the impression in MRI is classified as more severe and extensive. The reliability of rating intracranial impressions was low for both MRI and CT.

Currently, the workflow requires user intervention and accordingly the aim of fully automizing the workflow was not reached. Especially differentiation between air and bone tissue in the nasal and ear cavities is an issue, also difficult task for the human eye. This segmentation issue can probably be partly overcome by incorporating atlas-based segmentation.

Despite the higher cost and longer scan time of an MRI relative to CT, the benefit of the method is the ability to obtain valuable diagnostic images of the brain tissue in the same imaging session. Although, MRI is an non-ionizing modality, the anesthesia or sedation has been recognized as a potential risk (Andropoulos & Greene, 2017) and the risk-benefit aspect needs to be evaluated by physicians. Quite early on in this research project BB-MRI was used as the only diagnostic imaging modality, i.e. CT images were no-longer acquired. Thus, the number of inputs for statistical analysis is small in Study **IV**. This early change of imaging modality from CT to MRI advocates for the use of BB-MRI.

The BB-MRI sequence was optimized based on the results from the segmentation. The scan time of the final sequence was approximately 2 minutes, which outputs both IP and OOP images with a resolution of 0.5x0.5x0.9 mm (in-plane interpolation). For the bottle-fed protocol, the usability of the StarVibe sequence was assessed. The benefit of the StarVibe sequence is the significantly lower acoustic noise levels and tolerance to motion, which enables imaging of infants in natural sleep (Study **IV**). However, the resolution of the StarVibe sequence is currently lower than for the regular BB-MRI sequence and cannot be increased due to technical restriction. This is a disadvantage that needs to be overcome, because the skull structures of these infants are smaller, and the partial volume artifact will lead to misclassification in segmentation. The contrast of the StarVibe sequence is a bit different from the regular BB-MRI sequence and will also require sequence or algorithm optimization.

A clear limitation in the development of the algorithm is that the image segmentations were assessed only visually in the development stage and for only a few datasets at a time. Due to the sequence development and large variations in patient age, the acquired data are quite heterogenous. A more systematic assessment, with a higher number of patient data for investigation of the segmentations would probably have been beneficial. The segmentation algorithm has properties that might not be beneficial in some cases:

- Because the skull is the largest contiguous category, we removed all other smaller fragments to improve the segmentation. This might also remove correctly classified tissue.
- The fuzzy C-means clustering estimates the probabilities of belonging to a cluster also based on its neighborhood. The weighting of the neighborhood might lead to misclassifications of thin or small structure, which might especially affect the results when segmenting the skull of infants. The weighting of the neighborhood can be changed by the parameter α_w in Equation 11.
- Although the segmentation of the water only images was not useful in segmenting the skull, it can be beneficial in other application and areas, that are more difficult to image e.g. the neck, where B_0 homogeneity is a problem.

In Study **IV**, the inter-rater reliability of assessing intracranial impression was low from both BB-MRI and CT images. This suggests that the visual estimation of intracranial impressions is difficult. Introducing a method that could calculate skull thickness, might alleviate this issue. However, in this case reference values for the normal skull would be needed for different age groups.

Currently, all BB-MRI is performed on a 3T Philips Ingenia scanner at the New Children's Hospital. The sequence was easily transferred to the scanner from another vendor and the imaging could continue without delays. The sequence is still evolving, and adjustments have been made. The adjustments have been made based by visually assessing the output of the segmentation algorithm. The 3D Vane sequence on the Philips scanner, which corresponds to the Siemens StarVibe sequence, has not yet been tested and it will be interesting to determine whether a better resolution can be achieved. However, it must be noted that the Philips 3D Vane sequence is not a "quiet" sequence. The use of a less motion-sensitive sequence combined with modern in-bore video-viewing possibilities could enable imaging patients without anesthesia, reducing imaging costs. To develop of the post-processing, the current interest is in investigating the use of neural networks for segmentation. For the neural network algorithm, the images segmented for Studies **III** and **IV** will be used as teaching and validation material.

6.3 MULTI-CONTRAST IMAGING WITH GRADIENT ECHO PLURAL CONTRAST IMAGING

Study **V** revealed that with a PF factor of 6/8 and 7/8 in the phase direction, one can achieve a 24% and 10% reduction in scan time, respectively (Table 2). PF in the slice direction should not be used, because it will have an impact on the T_2* value, contrast, and slice thickness. This was more prominent with the 5 mm slice thickness than the 2 mm slice thickness. The clinical needs set the requirements for the image quality, and thus, the choice of imaging acceleration methods. Further reduction in scan time can be achieved by acquiring thicker slices or lower in-plane resolution.

The ACR phantom was not optimal for image quality assessment because there were severe Gibbs ringing artifacts due to boundaries and quantitative T_2^* reference values were not available. A relaxation phantom would have enabled us to assess multiple samples with different relaxation times in the same acquisition and hopefully with less artifacts. However, image quality could be assessed from the ACR phantom, which probably would not have been possible with the relaxation phantom. Of interest was also to quantitate the T_2^* value and phantoms for this purpose are not commercially available.

Before the measurements, it would have been possible to study the impact of PF with simulated data. However, the scanner reconstruction algorithm might make some alterations to the data, of which the user would be unaware, and the results from the simulations would need to be verified.

One must note that the image quality was assessed only from images of the first TE. The signal behavior might be different in the images acquired with larger TE values as the FID decays and the noise increase. This can affect the image quality and fitting of the decay model. The quantitative T_2* values were estimated with the least square method, which is known to be sensitive to noise (Otto et al., 2011). Thus, the use of other fitting methods must be explored. The scan time can probably also be reduced by acquiring less echoes. This would be an interesting subject for a future study.

7 CONCLUSION

In this thesis magnetic resonance imaging (MRI) and post-processing methods were assessed and developed with respect to safety, image quality and post-processing. All studies were motivated by the need to bring the methods to clinical practice.

Safety of simultaneous electroencephalography and functional MRI was assured and the impact of the equipment on image quality was assessed. The maximum temperature increase observed was 4.1ºC with the T_2-weighted turbo spin echo sequence, which does not exceed the 45ºC temperature limit set by the manufacturer if the electrode is at normal body temperature. The EEG equipment does not significantly affect the image quality. Artifacts up to 15 mm were observed in the phantom measurements, but these were not visible in the volunteer studies. An overall reduced SNR was noted in the volunteer studies when the EEG equipment was present.

A black bone (BB) MR protocol was developed for imaging infants with the feed-and-wrap technique and for older children with anesthesia. The final segmentation algorithm used in-phase and out-of-phase imaging and utilized the fuzzy c-means clustering with bias field correction. The BB-MRI 3D renderings were compared with CT images by experienced clinicians and radiologists. The BB-MRI findings were consistent with CT.

The relatively long scan time of the sequence used for gradient echo plural contrast imaging (GEPCI) postprocessing is a problem in clinical settings. Only the PF in the phase encoding direction should be used and this can shorten the scan time by approx. 24 %.

Currently, at our institution, simultaneous EEG-fMRI and BB-MRI are in routine clinical practice. The GEPCI post-processing technique is undergoing evaluation and has been used in two research protocols.

8 REFERENCES

Abdel-Rehim, S., Bagirathan, S., Al-Benna, S., & O'Boyle, C. (2014). Burns from ECG leads in an MRI scanner: Case series and discussion of mechanisms. *Annals of Burns and Fire Disasters*, *27*(4), 215–218. http://www.ncbi.nlm.nih.gov/pubmed/26336370

Agrawal, D., Steinbok, P., & Cochrane, D. D. (2007). Significance of beaten copper appearance on skull radiographs in children with isolated sagittal synostosis. *Child's Nervous System*, *23*(12), 1467–1470. https://doi.org/10.1007/s00381-007-0430-6

Ahmed, M. N., Yamany, S. M., Mohamed, N., Farag, A. A., & Moriarty, T. (2002). A modified fuzzy C-means algorithm for bias field estimation and segmentation of MRI data. *IEEE Transactions on Medical Imaging*, *21*(3), 193–199. https://doi.org/10.1109/42.996338

Albright, A. L., & Byrd, R. P. (1981). Suture pathology in craniosynostosis. *Journal of Neurosurgery*, *54*(3), 384–387. https://doi.org/10.3171/jns.1981.54.3.0384

Alibek, S., Vogel, M., Sun, W., Winkler, D., Baker, C. A., Burke, M., & Gloger, H. (2014). Acoustic noise reduction in MRI using Silent Scan: An initial experience. *Diagnostic and Interventional Radiology*, *20*(4), 360–363. https://doi.org/10.5152/dir.2014.13458

Allen, P. J., Josephs, O., & Turner, R. (2000). *A Method for Removing Imaging Artifact from Continuous EEG Recorded during Functional MRI*. https://doi.org/10.1006/nimg.2000.0599

American College of Radiology. (2005). *Radiology, Phantom Test Guidance for the ACR MRI Accreditation Program*. https://www.acraccreditation.org/

Andropoulos, D. B., & Greene, M. F. (2017). Anesthesia and developing brains - Implications of the FDA warning. In *New England Journal of Medicine* (Vol. 376, Issue 10, pp. 905–907). Massachussetts Medical Society. https://doi.org/10.1056/NEJMp1700196

Angelone, L. M., Potthast, A., Segonne, F., Iwaki, S., Belliveau, J. W., & Bonmassar, G. (2004). Metallic electrodes and leads in simultaneous EEG-MRI: specific absorption rate (SAR) simulation studies. *Bioelectromagnetics*, *25*(4), 285–295. https://doi.org/10.1002/bem.10198

Angelone, L. M., Vasios, C. E., Wiggins, G., Purdon, P. L., & Bonmassar, G. (2006). On the effect of resistive EEG electrodes and leads during 7 T MRI: simulation and temperature measurement studies. *Magnetic Resonance Imaging*, *24*(6), 801–812. https://doi.org/10.1016/j.mri.2006.01.006

Baker, K. B., Tkach, J. A., Nyenhuis, J. A., Phillips, M., Shellock, F. G., Gonzalez-Martinez, J., & Rezai, A. R. (2004). Evaluation of Specific Absorption Rate as a Dosimeter of MRI-Related Implant Heating. *J. Magn. Reson. Imaging*, *20*, 315–320. https://doi.org/10.1002/jmri.20103

Bashir, A., & Yablonskiy, D. A. (2006). Gradient Echo Plural Contrast Imaging (GEPCI). *In Vivo*, *428*(2000), 2006–2006. https://afni.nimh.nih.gov/sscc/staff/rwcox/ISMRM_2006/ISMRM 2006 - 3340/files/00429.pdf

Berker, Y., Franke, J., Salomon, A., Palmowski, M., Donker, H. C. W., Temur, Y., Mottaghy, F. M., Kuhl, C., Izquierdo-Garcia, D., Fayad, Z. A., Kiessling, F., &

Schulz, V. (2012). MRI-based attenuation correction for hybrid PET/MRI Systems: A 4-class tissue segmentation technique using a combined ultrashort-echo-time/Dixon MRI sequence. *Journal of Nuclear Medicine*, *53*(5), 796–804. https://doi.org/10.2967/jnumed.111.092577

Bezdek, J. C., Ehrlich, R., & Full, W. (1984). FCM: The fuzzy c-means clustering algorithm. *Computers and Geosciences*, *10*(2–3), 191–203. https://doi.org/10.1016/0098-3004(84)90020-7

Bonmassar, G., Hadjikhani, N., Ives, J. R., Hinton, D., & Belliveau, J. W. (2001). Influence of EEG electrodes on the BOLD fMRI signal. *Human Brain Mapping*, *14*(2), 108–115. https://doi.org/10.1002/hbm

Brain Products. (2008). Important safety aspects for combined MR recordings. *Brain Producst New Letter*, *3*, 7–9.

Brenner, D. J., Hall, E. J., & Phil, D. (2007). Computed Tomography-An Increasing Source of Radiation Exposure. In *N Engl J Med* (Vol. 357). www.nejm.org

Brueggen, K., Fiala, C., Berger, C., Ochmann, S., Babiloni, C., & Teipel, S. J. (2017). Early changes in alpha band power and DMN BOLD activity in Alzheimer's disease: A simultaneous resting state EEG-fMRI study. *Frontiers in Aging Neuroscience*, *9*(OCT). https://doi.org/10.3389/fnagi.2017.00319

Bushberg, J., Seibert, J., & Leidholdt, E. (2002). *Essential Physics of Medical Imaging* (2nd ed.). Lipincott.

Carmichael, D. W., Thornton, J. S., Rodionov, R., Thornton, R., McEvoy, A. W., Ordidge, R. J., Allen, P. J., & Lemieux, L. (2010). Feasibility of simultaneous intracranial EEG-fMRI in humans: a safety study. *NeuroImage*, *49*(1), 379–390. https://doi.org/10.1016/j.neuroimage.2009.07.062

Chandarana, H., Block, T. K., Rosenkrantz, A. B., Lim, R. P., Kim, D., Mossa, D. J., Babb, J. S., Kiefer, B., & Lee, V. S. (2011). Free-Breathing Radial 3D Fat-Suppressed T1-Weighted Gradient Echo Sequence A Viable Alternative for Contrast-Enhanced Liver Imaging in Patients Unable to Suspend Respiration. In *Investigative Radiology* • (Vol. 46, Issue 10).

Collins, C. M., & Smith, M. B. (2001). Calculations of B1 distribution, SNR, and SAR for a surface coil adjacent to an anatomically-accurate human body model. *Magnetic Resonance in Medicine*, *45*(4), 692–699. https://doi.org/10.1002/mrm.1092

Debener, S., Mullinger, K. J., Niazy, R. K., & Bowtell, R. W. (2008). Properties of the ballistocardiogram artefact as revealed by EEG recordings at 1.5, 3 and 7 T static magnetic field strength. *International Journal of Psychophysiology*, *67*(3), 189–199. https://doi.org/10.1016/j.ijpsycho.2007.05.015

Debener, S., Ullsperger, M., Siegel, M., & Engel, A. K. (2006a). Single-trial EEG-fMRI reveals the dynamics of cognitive function. *Trends in Cognitive Sciences*, *10*(12), 558–563. https://doi.org/10.1016/j.tics.2006.09.010

Debener, S., Ullsperger, M., Siegel, M., & Engel, A. K. (2006b). Single-trial EEG–fMRI reveals the dynamics of cognitive function. *Trends in Cognitive Sciences*, *10*(12), 558–563. https://doi.org/10.1016/j.tics.2006.09.010

Dixon, W. T. (1984). Simple proton spectroscopic imaging. *Radiology*, *153*(1), 189–194. https://doi.org/10.1148/radiology.153.1.6089263

Dong, L., Luo, C., Zhu, Y., Hou, C., Jiang, S., Wang, P., Biswal, B. B., & Yao, D. (2016). Complex discharge-affecting networks in juvenile myoclonic epilepsy: A simultaneous EEG-fMRI study. *Human Brain Mapping*, *37*(10), 3515–3529. https://doi.org/10.1002/hbm.23256

Dunn, J. C. (1973). A fuzzy relative of the ISODATA process and its use in detecting compact well-separated clusters. *Journal of Cybernetics*, *3*(3), 32–57. https://doi.org/10.1080/01969727308546046

Ehman, R. L., & Felmlee, J. P. (1989). Adaptive technique for high-definition MR imaging of moving structures. *Radiology*, *173*(1), 255–263. https://doi.org/10.1148/radiology.173.1.2781017

Eley, K. A., McIntyre, A. G., Watt-Smith, S. R., & Golding, S. J. (2012). "Black bone" MRI: a partial flip angle technique for radiation reduction in craniofacial imaging. *The British Journal of Radiology*, *85*(1011), 272–278. https://doi.org/10.1259/bjr/95110289

Eley, K. A., Watt-Smith, S. R., & Golding, S. J. (2012). "Black bone" MRI: a potential alternative to CT when imaging the head and neck: report of eight clinical cases and review of the Oxford experience. *The British Journal of Radiology*, *85*(1019), 1457–1464. https://doi.org/10.1259/bjr/16830245

Eley, K. A., Watt-Smith, S. R., Sheerin, F., & Golding, S. J. (2014). "Black Bone" MRI: a potential alternative to CT with three-dimensional reconstruction of the craniofacial skeleton in the diagnosis of craniosynostosis. *European Radiology*, *24*(10), 2417–2426. https://doi.org/10.1007/s00330-014-3286-7

Eley, Sheerin, F., Taylor, N., Watt-Smith, S. R., & Golding, S. J. (2013). Identification of normal cranial sutures in infants on routine magnetic resonance imaging. *Journal of Craniofacial Surgery*, *24*(1), 317–320. https://doi.org/10.1097/SCS.0b013e318275edee

Fagan, A. M., Hassenstab, J., Cairns, N. J., Morris, J. C., Morris, J. C., Christensen, J. J., & Yablonskiy, D. A. (2017). In vivo detection of microstructural correlates of brain pathology in preclinical and early Alzheimer Disease with magnetic resonance imaging. *NeuroImage*, *148*, 296–304. https://doi.org/10.1016/j.neuroimage.2016.12.026

Fearon, J. A., Singh, D. J., Beals, S. P., & Yu, J. C. (2007). The Diagnosis and Treatment of Single-Sutural Synostoses: Are Computed Tomographic Scans Necessary? *Plastic and Reconstructive Surgery*, *120*(5), 1327–1331. https://doi.org/10.1097/01.prs.0000279477.56044.55

Fedorov, A., Beichel, R., Kalpathy-Cramer, J., Finet, J., Fillion-Robin, J. C., Pujol, S., Bauer, C., Jennings, D., Fennessy, F., Sonka, M., Buatti, J., Aylward, S., Miller, J. V., Pieper, S., & Kikinis, R. (2012). 3D Slicer as an image computing platform for the Quantitative Imaging Network. *Magnetic Resonance Imaging*, *30*(9), 1323–1341. https://doi.org/10.1016/j.mri.2012.05.001

Friedman, L., & Glover, G. H. (2006). Report on a multicenter fMRI quality assurance protocol. *Journal of Magnetic Resonance Imaging*, *23*(6), 827–839. https://doi.org/10.1002/jmri.20583

Frush, D. P., Donnelly, L. F., & Rosen, N. S. (2003). Computed tomography and radiation risks: What pediatric health care providers should know. In *Pediatrics* (Vol. 112, Issue 4, pp. 951–957). https://doi.org/10.1542/peds.112.4.951

Heismann, B., Ott, M., & Grodzki, D. (2015). Sequence-based acoustic noise reduction of clinical MRI scans. *Magnetic Resonance in Medicine*, *73*(3), 1104–1109. https://doi.org/10.1002/mrm.25229

Hukki, A., Koljonen, V., Karppinen, A., Valanne, L., & Leikola, J. (2012). Brain anomalies in 121 children with non-syndromic single suture craniosynostosis by MR imaging. *European Journal of Paediatric Neurology*, *16*(6), 671–675. https://doi.org/10.1016/j.ejpn.2012.04.003

International Electrochemical Commission. (2010). Medical electrical equipment: part 2-33. Particular requirements for the safety of magnetic resonance equipment for medical diagnosis. In *IEC 60601-2-33*. https://doi.org/10.5594/J09750

International Electrotechnical Commission. (2005). *IEC 60601-1:2005 Medical electrical equipment - Part 1: General requirements for basic safety and essential performance*. https://webstore.iec.ch/publication/2612

Ives, J. R., Warach, S., Schmitt, F., Edelman, R. R., & Schomer, D. L. (1993). Monitoring the patient's EEG during echo planar MRI. *Electroencephalography and Clinical Neurophysiology*, *87*(6), 417–420. https://doi.org/10.1016/0013-4694(93)90156-P

Jezzard, P., Matthews, P. M., & Smith, S. M. (2003). *Functional Magnetic Resonance Imaging: An Introduction to Methods*. OUP Oxford.

Jin, J.-M. (1998). *Electromagnetic analysis and design in magnetic resonance imaging*. CRC Press.

Johnstone, E., Wyatt, J. J., Henry, A. M., Short, S. C., Sebag-Montefiore, D., Murray, L., Kelly, C. G., McCallum, H. M., & Speight, R. (2018). Systematic Review of Synthetic Computed Tomography Generation Methodologies for Use in Magnetic Resonance Imaging–Only Radiation Therapy. In *International Journal of Radiation Oncology Biology Physics* (Vol. 100, Issue 1, pp. 199–217). Elsevier Inc. https://doi.org/10.1016/j.ijrobp.2017.08.043

Kim, J. H., Lee, J. S., Song, I. C., & Lee, D. S. (2012). Comparison of segmentation-based attenuation correction methods for PET/MRI: Evaluation of bone and liver standardized uptake value with oncologic PET/CT data. *Journal of Nuclear Medicine*, *53*(12), 1878–1882. https://doi.org/10.2967/jnumed.112.104109

Kirmi, O., Lo, S. J., Johnson, D., & Anslow, P. (2009). Craniosynostosis: A Radiological and Surgical Perspective. *Seminars in Ultrasound, CT and MRI*, *30*(6), 492–512. https://doi.org/10.1053/j.sult.2009.08.002

Koopmans, P. J., Boyacioğlu, R., Barth, M., & Norris, D. G. (2012). Whole brain, high resolution spin-echo resting state fMRI using PINS multiplexing at 7 T. *NeuroImage*, *62*(3), 1939–1946. https://doi.org/10.1016/J.NEUROIMAGE.2012.05.080

Korhonen, J., Kapanen, M., Keyriläinen, J., Seppälä, T., & Tenhunen, M. (2014). A dual model HU conversion from MRI intensity values within and outside of bone segment for MRI-based radiotherapy treatment planning of prostate cancer. *Medical Physics*, *41*(1). https://doi.org/10.1118/1.4842575

Krakow, K., Allen, P. J., Symms, M. R., Lemieux, L., Josephs, O., & Fish, D. R. (2000). EEG recording during fMRI experiments: image quality. *Human Brain Mapping*, *10*(1), 10–15. http://www.ncbi.nlm.nih.gov/pubmed/10843514

Kroon, D.-J. (2020). *Bias Field Corrected Fuzzy C-Means - File Exchange - MATLAB Central*. MATLAB Central File Exchange. https://se.mathworks.com/matlabcentral/fileexchange/25712-bias-field-corrected-fuzzy-c-means

Kuusela, L., Turunen, S., Valanne, L., & Sipilä, O. (2015). Safety in simultaneous EEG-fMRI at 3 T: temperature measurements. *Acta Radiologica*, *56*(6), 739–745. https://doi.org/10.1177/0284185114536385

Lazeyras, F., Zimine, I., Blanke, O., Perrig, S. H., & Seeck, M. (2001). Functional MRI with simultaneous EEG recording: feasibility and application to motor and visual activation. *Journal of Magnetic Resonance Imaging : JMRI*, *13*(6), 943–948.

Leikola, J., Koljonen, V., Valanne, L., & Hukki, J. (2010). The incidence of Chiari malformation in nonsyndromic, single suture craniosynostosis. *Child's Nervous System*, *26*(6), 771–774. https://doi.org/10.1007/s00381-009-1044-y

Lemieux, L., Allen, P. J., Franconi, F., Symms, M. R., & Fish, D. R. (1997). Recording of EEG during fMRI experiments: patient safety. *Magnetic Resonance in Medicine : Official Journal of the Society of Magnetic Resonance in Medicine / Society of Magnetic Resonance in Medicine*, *38*(6), 943–952.

Li, F., Tao, Q., Peng, W., Zhang, T., Si, Y., Zhang, Y., Yi, C., Biswal, B., Yao, D., & Xu, P. (2020). Inter-subject P300 variability relates to the efficiency of brain networks reconfigured from resting- to task-state: Evidence from a simultaneous event-related EEG-fMRI study. *NeuroImage*, *205*, 116285. https://doi.org/10.1016/j.neuroimage.2019.116285

Luo, J., Jagadeesan, B. D., Cross, A. H., & Yablonskiy, D. A. (2012). Gradient Echo Plural Contrast Imaging - Signal model and derived contrasts: T2 *, T1, Phase, SWI, T1f, FST2 *and T2 *-SWI. *NeuroImage*, *60*(2), 1073–1082. https://doi.org/10.1016/j.neuroimage.2012.01.108

Luo, J., Yablonskiy, D. A., Hildebolt, C. F., Lancia, S., & Cross, A. H. (2014). Gradient echo magnetic resonance imaging correlates with clinical measures and allows visualization of veins within multiple sclerosis lesions. *Multiple Sclerosis Journal*, *20*(3), 349–355. https://doi.org/10.1177/1352458513495935

Mäkelä, T., Ihalainen, T., & Sipilä, O. (2012). Automated analysis of ACR phantom images. *29th Annual Scientific Meeting of the European Society for Magnetic Resonance in Medicine and Biology*.

Martínez-Cagigal, V. (2019). *Topographic EEG/MEG plot - File Exchange - MATLAB Central*. https://se.mathworks.com/matlabcentral/fileexchange/72729-topographic-eeg-meg-plot

Mattei, E., Triventi, M., Calcagnini, G., Censi, F., Kainz, W., Mendoza, G., Bassen, H. I., & Bartolini, P. (2008). Complexity of MRI induced heating on metallic leads: experimental measurements of 374 configurations. *Biomedical Engineering Online*, *7*, 11. https://doi.org/10.1186/1475-925X-7-11

McRobbie, W., Moore, E. A., Graves, M. J., & Prince, M. R. (2005). *MRI: From Picture to Proton*. Cambridge.

Meriläinen, V. (2002). *Magnetic resonance imaging with simultanous electroencephalography recordings: safety issues*. Helsinki University of Technology, Department of Electrical and Communication Engingeering.

Michels, L., Bucher, K., Lüchinger, R., Klaver, P., Martin, E., Jeanmonod, D., & Brandeis, D. (2010). Simultaneous EEG-fMRI during a Working Memory Task: Modulations in Low and High Frequency Bands. *PLoS ONE*, *5*(4), e10298. https://doi.org/10.1371/journal.pone.0010298

Mullinger, K., Brookes, M., Stevenson, C., Morgan, P., & Bowtell, R. (2008). Exploring the feasibility of simultaneous electroencephalography/functional magnetic resonance imaging at 7 T. *Proceedings of the International School on Magnetic Resonance and Brain Function*, *26*(7), 968–977. https://doi.org/10.1016/j.mri.2008.02.014

Mullinger, K., Debener, S., Coxon, R., & Bowtell, R. (2008). Effects of simultaneous EEG recording on MRI data quality at 1.5, 3 and 7 tesla. *International Journal of Psychophysiology*, *67*(3), 178–188. https://doi.org/10.1016/j.ijpsycho.2007.06.008

Nagaraja, S., Anslow, P., & Winter, B. (2013). Craniosynostosis. In *Clinical*

Radiology (Vol. 68, Issue 3, pp. 284–292). W.B. Saunders. https://doi.org/10.1016/j.crad.2012.07.005

Negishi, M., Abildgaard, M., Laufer, I., Nixon, T., & Constable, R. T. (2008). An EEG (electroencephalogram) recording system with carbon wire electrodes for simultaneous EEG-fMRI (functional magnetic resonance imaging) recording. *Journal of Neuroscience Methods*, *173*(1), 99–107. https://doi.org/10.1016/j.jneumeth.2008.05.024

Norris, D. G., Koopmans, P. J., Boyacioğlu, R., & Barth, M. (2011). Power independent of number of slices (PINS) radiofrequency pulses for low-power simultaneous multislice excitation. *Magnetic Resonance in Medicine*, *66*(5), 1234–1240. https://doi.org/10.1002/mrm.23152

Nöth, U., Laufs, H., Stoermer, R., & Deichmann, R. (2012). Simultaneous electroencephalography-functional MRI at 3 T: An analysis of safety risks imposed by performing anatomical reference scans with the EEG equipment in place. *Journal of Magnetic Resonance Imaging*, *35*(3), 561–571. https://doi.org/10.1002/jmri.22843

Otto, R., Ferguson, M. R., Marro, K., Grinstead, J. W., & Friedman, S. D. (2011). Limitations of using logarithmic transformation and linear fitting to estimate relaxation rates in iron-loaded liver. *Pediatric Radiology*, *41*(10), 1259–1265. https://doi.org/10.1007/s00247-011-2082-7

Parker, D. L., Payne, A., Todd, N., & Hadley, J. R. (2014). Phase reconstruction from multiple coil data using a virtual reference coil. *Magnetic Resonance in Medicine*, *72*(2), 563–569. https://doi.org/10.1002/mrm.24932

Partanen, J., & Cheour, M. (2006). *Kliininen neurofysiologia*. Duodecim.

Pearce, M. S., Salotti, J. A., Little, M. P., McHugh, K., Lee, C., Kim, K. P., Howe, N. L., Ronckers, C. M., Rajaraman, P., Craft, A. W., Parker, L., & De González, A. B. (2012). Radiation exposure from CT scans in childhood and subsequent risk of leukaemia and brain tumours: A retrospective cohort study. *The Lancet*, *380*(9840), 499–505. https://doi.org/10.1016/S0140-6736(12)60815-0

Persing, J. A. (2008). MOC-PS(SM) CME Article: Management Considerations in the Treatment of Craniosynostosis. *Plastic and Reconstructive Surgery*, *121*(Supplement), 1–11. https://doi.org/10.1097/01.prs.0000305929.40363.bf

Pipe, J. G. (1999). Motion Correction With PROPELLER MRI: Application to Head Motion and Free-Breathing Cardiac Imaging. In *Magnetic Resonance in Medicine* (Vol. 42).

Quirk, J. D., Sukstanskii, A. L., Bretthorst, G. L., & Yablonskiy, D. A. (2009). Optimal decay rate constant estimates from phased array data utilizing joint Bayesian analysis. *Journal of Magnetic Resonance*, *198*(1), 49–56. https://doi.org/10.1016/j.jmr.2009.01.001

Ruuth, R., Kuusela, L., Mäkelä, T., Melkas, S., & Korvenoja, A. (2019). Comparison of reconstruction and acquisition choices for quantitative T2* maps and synthetic contrasts. *European Journal of Radiology Open*, *6*, 42–48. https://doi.org/10.1016/j.ejro.2018.12.006

Sammet, S. (2016). Magnetic resonance safety. *Abdominal Radiology*, *41*(3), 444–451. https://doi.org/10.1007/s00261-016-0680-4

Sati, P., Cross, A. H., Luo, J., Hildebolt, C. F., & Yablonskiy, D. A. (2010). In vivo quantitative evaluation of brain tissue damage in multiple sclerosis using gradient echo plural contrast imaging technique. *NeuroImage*, *51*(3), 1089–1097. https://doi.org/10.1016/j.neuroimage.2010.03.045

Shellock, F. G. (2001). *Magnetic resonance procedures : health effects and safety*. CRC Press.

Shellock, F. G., & Bradley, W. G. (2000). Magnetic resonance procedures: Health effects and safety. In *Magnetic Resonance Procedures: Health Effects and Safety*. https://doi.org/10.1118/1.1603741

Simmons, A., Moore, E., & Williams, S. C. R. (1999). Quality control for functional magnetic resonance imaging using automated data analysis and Shewhart charting. *Magnetic Resonance in Medicine*, *41*(6), 1274–1278. https://doi.org/10.1002/(SICI)1522-2594(199906)41:6<1274::AID-MRM27>3.0.CO;2-1

Sled, J. G., & Bruce Pike, G. (1998). Standing-Wave and RF Penetration Artifacts Caused by Elliptic Geometry: An Electrodynamic Analysis of MRI. *IEEE Transactions on Medical Imaging*, *17*(4), 653–662. https://doi.org/10.1109/42.730409

Toennies, K. D. (2017). *Advances in Computer Vision and Pattern Recognition Guide to Medical Image Analysis*. http://www.springer.com/series/4205

Tuite, G. F., Evanson, J., Chong, W. K., Thompson, D. N. P., Harkness, W. F., Jones, B. M., & Hayward, R. D. (1996). The beaten copper cranium: A correlation between intracranial pressure, cranial radiographs, and computed tomographic scans in children with craniosynostosis. *Neurosurgery*, *39*(4), 691–699. https://doi.org/10.1097/00006123-199610000-00007

Uji, M., Wilson, R., Francis, S. T., Mullinger, K. J., & Mayhew, S. D. (2018). Exploring the advantages of multiband fMRI with simultaneous EEG to investigate coupling between gamma frequency neural activity and the BOLD response in humans. *Human Brain Mapping*. https://doi.org/10.1002/hbm.23943

Ullsperger, M., & Debener, S. (2010). *Simultaneous EEG and fMRI*. Oxford University Press. https://doi.org/10.1093/acprof:oso/9780195372731.001.0001

Vannier, M. W., Hildebolt, C. F., Marsh, J. L., Pilgram, T. K., McAlister, W. H., Shackelford, G. D., Offutt, C. J., & Knapp, R. H. (1989). Craniosynostosis: Diagnostic value of three-dimensional CT reconstruction. *Radiology*, *173*(3), 669–673. https://doi.org/10.1148/radiology.173.3.2813770

Vasios, C. E., Angelone, L. M., Purdon, P. L., Ahveninen, J., Belliveau, J. W., & Bonmassar, G. (2006). EEG/(f)MRI measurements at 7 Tesla using a new EEG cap ("InkCap"). *NeuroImage*, *33*(4), 1082–1092. https://doi.org/10.1016/J.NEUROIMAGE.2006.07.038

Wang, H., Chandarana, H., Block, K. T., Vahle, T., Fenchel, M., & Das, I. J. (2017). Dosimetric evaluation of synthetic CT for magnetic resonance-only based radiotherapy planning of lung cancer. *Radiation Oncology*, *12*(1). https://doi.org/10.1186/s13014-017-0845-5

Wen, J., Yablonskiy, D. A., Luo, J., Lancia, S., Hildebolt, C., & Cross, A. H. (2015). Detection and quantification of regional cortical gray matter damage in multiple sclerosis utilizing gradient echo MRI. *NeuroImage: Clinical*, *9*, 164–175. https://doi.org/10.1016/j.nicl.2015.08.003

White, M. (2016). *MetaPost MRI pulse sequence macros*. https://bitbucket.org/mjwhite/pulses

Wong, E. (2012). Optimized Phase Schedules for Minimizing Peak RF Power in Simultaneous Multi-Slice RF Excitation Pulses. *ISMRM 20th Annual Meeting*, 2209. http://dev.ismrm.org/2012/2209.html

Yablonskiy, D. A., Sukstanskii, A. L., Luo, J., & Wang, X. (2013). Voxel spread

function method for correction of magnetic field inhomogeneity effects in quantitative gradient-echo-based MRI. *Magnetic Resonance in Medicine*, *70*(5), 1283–1292. https://doi.org/10.1002/mrm.24585

Yeung, C. J., Susil, R. C., & Atalar, E. (2002). RF safety of wires in interventional MRI: using a safety index. *Magnetic Resonance in Medicine*, *47*(1), 187–193. http://www.ncbi.nlm.nih.gov/pubmed/11754458

Zhu, X., Ye, J., Bao, Z., Luo, X., Zhu, Q., Shang, S., Dou, W., & Xia, W. (2020). Benefits of Silent DWI MRI in Success Rate, Image Quality, and the Need for Secondary Sedation During Brain Imaging of Children of 3–36 Months of Age. *Academic Radiology*, *27*(4), 543–549. https://doi.org/10.1016/j.acra.2019.09.022

Zich, C., Debener, S., Kranczioch, C., Bleichner, M. G., Gutberlet, I., & De Vos, M. (2015). Real-time EEG feedback during simultaneous EEG-fMRI identifies the cortical signature of motor imagery. *NeuroImage*, *114*, 438–447. https://doi.org/10.1016/j.neuroimage.2015.04.020

Zotev, V., Phillips, R., Misaki, M., Wong, C. K., Wurfel, B. E., Krueger, F., Feldner, M., & Bodurka, J. (2018). Real-time fMRI neurofeedback training of the amygdala activity with simultaneous EEG in veterans with combat-related PTSD. *NeuroImage: Clinical*, *19*, 106–121. https://doi.org/10.1016/j.nicl.2018.04.010